



Title	Effect of degree of substitution on the microphase separation and mechanical properties of cellooligosaccharide acetate-based elastomers
Author(s)	Katsuhara, Satoshi; Sunagawa, Naoki; Igarashi, Kiyohiko; Takeuchi, Yutaka; Takahashi, Kenji; Yamamoto, Takuya; Li, Feng; Tajima, Kenji; Isono, Takuya; Satoh, Toshifumi
Citation	Carbohydrate Polymers, 316, 120976 https://doi.org/10.1016/j.carbpol.2023.120976
Issue Date	2023-09-15
Doc URL	http://hdl.handle.net/2115/92207
Rights	© <2023>. This manuscript version is made available under the CC-BY-NC-ND 4.0 license http://creativecommons.org/licenses/by-nc-nd/4.0/
Rights(URL)	http://creativecommons.org/licenses/by-nc-nd/4.0/
Type	article (author version)
File Information	Carbohydrate Polymers 316 120976 .pdf



[Instructions for use](#)

1 **Effect of degree of substitution on the microphase separation and mechanical properties of**
2 **cellooligosaccharide acetate-based elastomers**

3 Satoshi Katsuhara,^a Naoki Sunagawa,^b Kiyohiko Igarashi,^{b,c} Yutaka Takeuchi,^d Kenji Takahashi,^e
4 Takuya Yamamoto,^f Feng Li,^f Kenji Tajima, ^{*,f} Takuya Isono, ^{*,f} Toshifumi Satoh^{*,f}

5
6 *^aGraduate School of Chemical Sciences and Engineering, Hokkaido University, Sapporo 060-8628,*
7 *Japan*

8 *^bDepartment of Biomaterial Sciences, Graduate School of Agriculture and Life Sciences, The*
9 *University of Tokyo, Tokyo 113-8657, Japan*

10 *^cVTT Technical Research Centre of Finland Ltd., VTT FI-02044, Finland*

11 *^dNoto Center for Fisheries Science and Technology, Faculty of Biological Science and Technology,*
12 *Kanazawa University, Noto-cho, Ishikawa 927-0552, Japan*

13 *^eFaculty of Biological Science and Technology, Institute of Science and Engineering, Kanazawa*
14 *University, Kanazawa 920-1192, Japan*

15 *^fFaculty of Engineering, Hokkaido University, Sapporo 060-8628, Japan*

16

17 **Corresponding Authors**

18 Kenji Tajima – *Faculty of Engineering, Hokkaido University, Sapporo 060-8628, Japan; ORCID*
19 *0000-0003-3764-2084; Email: ktajima@eng.hokudai.ac.jp; Phone number: +81-11-706-6567*

20 Takuya Isono – *Faculty of Engineering, Hokkaido University, Sapporo 060-8628, Japan; ORCID*
21 *0000-0003-3746-2084; Email: isono.t@eng.hokudai.ac.jp; Phone number: +81-11-706-2290*

22 Toshifumi Satoh – *Faculty of Engineering, Hokkaido University, Sapporo 060-8628, Japan;*
23 *ORCID 0000-0001-5449-9642; Email: satoh@eng.hokudai.ac.jp; Phone number: +81-11-706-6602*

24

25

26

27 **Abstract**

28 Thermoplastic elastomers (TPEs) have long been used in a wide range of industries.
29 However, most existing TPEs are petroleum-derived polymers. To realize environmentally benign
30 alternatives to conventional TPEs, cellulose acetate is a promising TPE hard segment because of its
31 sufficient mechanical properties, availability from renewable sources, and biodegradability in
32 natural environments. Because the degree of substitution (DS) of cellulose acetate governs a range
33 of physical properties, it is a useful parameter for designing novel cellulose acetate-based TPEs. In
34 this study, we synthesized cellulose acetate-based ABA-type triblock copolymers (AcCel_x-*b*-PDL-*b*-
35 AcCel_x) containing a celooligosaccharide acetate hard A segment (AcCel_x, where x is the DS; x =
36 3.0, 2.6, and 2.3) and a poly(δ -decanolactone) (PDL) soft B segment. Small-angle X-ray scattering
37 showed that decreasing the DS of AcCel_x-*b*-PDL-*b*-AcCel_x resulted in the formation of a more
38 ordered microphase-separated structure. Owing to the microphase separation of the hard cellulosic
39 and soft PDL segments, all the AcCel_x-*b*-PDL-*b*-AcCel_x samples exhibited elastomer-like
40 properties. Moreover, the decrease in DS improved toughness and suppressed stress relaxation.
41 Furthermore, preliminary biodegradation tests in an aqueous environment revealed that the decrease
42 in DS endowed AcCel_x-*b*-PDL-*b*-AcCel_x with greater biodegradability potential. This work
43 demonstrates the usefulness of cellulose acetate-based TPEs as next-generation sustainable
44 materials.

45 **Keywords:** thermoplastic elastomer, cellulose acetate, mechanical properties, biodegradability,
46 microphase separation, self-assembly

47

48 1. Introduction

49 Thermoplastic elastomers (TPEs) are essential materials in daily life and have been used in
50 various fields. The hot-melt processability and reusability of TPEs are major advantages over
51 conventional vulcanized rubbers, the thermoset nature of which prevents recycling. Most TPEs are
52 ABA-type triblock copolymers, where the A block is an amorphous or semicrystalline polymer with
53 a high glass transition temperature (T_g) and the B block is an amorphous rubbery polymer with a
54 low T_g . Microphase separation into the “hard” A domain and the “soft” B matrix plays a key role in
55 the elastic properties, with the hard A segments serving as physical crosslinks for the rubbery B
56 chains. Commonly, TPEs utilize polystyrene (PS) as the hard segment, and various PS-based TPEs
57 have been commercialized, as exemplified by PS-*b*-polyisoprene-*b*-PS, PS-*b*-polybutadiene-*b*-PS,
58 and PS-*b*-polyethylenepropylene-*b*-PS (Maji & Naskar, 2022). However, these TPEs are derived
59 from petroleum and lack biodegradability. Considering the recent demand for bio-based and
60 biodegradable plastics, it is necessary to develop new environmentally benign TPEs. Various
61 research groups have investigated bio-based and biodegradable alternatives to PS-based TPEs. For

Abbreviations: thermoplastic elastomer (TPE), glass transition temperature (T_g), polystyrene (PS), polylactide (PLA), block copolymer (BCP), poly(δ -decalactone) (PDL), degree of substitution (DS), tetrahydrofuran (THF), cellulose acetate (AcCel_x), small-angle X-ray scattering (SAXS), atomic force microscopy (AFM), propargyl-functionalized cellooligosaccharide (Cel-C≡CH), cellodextrin phosphorylase (CDP), α -D-glucose-1-phosphate (α G1P), dispersity (D), degree of polymerization (DP), matrix-assisted laser desorption/ionization time-of-flight mass spectrometry (MALDI-TOF MS), size-exclusion chromatography (SEC), differential scanning calorimetry (DSC), thermogravimetric analysis (TGA), wide-angle X-ray diffraction (WAXD), body-centered cubic (BCC), fast Fourier transform (FFT), order–disorder temperature (T_{ODT}), full width at half maximum (FWHM), Flory–Huggins interaction parameter (χ), Young’s modulus (E), strain at break (ϵ_b), stress at break (σ_b), hexagonal cylinder (HEX), scanning electron microscopy (SEM)

62 instance, TPEs with polylactide (PLA) hard segments combined with amorphous and low- T_g
63 aliphatic polyesters such as poly(β -methyl- δ -valerolactone), poly(ϵ -decalactone), and
64 poly(menthane) as soft segments have been fabricated (Fournier, Riversa, & Hillmyer, 2022;
65 Liffland & Hillmyer, 2021; Martello, Schneiderman, & Hillmyer, 2014; Shin et al., 2011; Watts &
66 Hillmyer, 2019; Watts, Kurokawa, & Hillmyer, 2017).

67 Most bio-based TPEs utilize PLA as the hard segment, but poly-/oligosaccharides have
68 potential as novel biodegradable hard segments. From a physiochemical point of view,
69 oligosaccharides are highly attractive hard domains because of their reasonable solubility, high T_g
70 (>100 °C), rigidity, and strong intermolecular interactions via hydrogen bonding or crystallization.
71 Advantageously, oligosaccharides are also strongly incompatible with hydrophobic polymers,
72 which leads to the formation of microphase-separated structures. Our previous study revealed that
73 block copolymers (BCPs) consisting of maltooligosaccharide with a wide variety of hydrophobic
74 polymers such as PS, poly(ϵ -caprolactone), poly(propylene oxide), polydimethylsiloxane, and
75 oligoisoprene self-assembled into highly ordered microphase-separated structures with domain
76 spacings (d) of less than 10 nm (Isono et al., 2013, 2019, 2022; Isono, Komaki, et al., 2020;
77 Katsuhara et al., 2020; Mumtaz et al., 2020; Nishimura et al., 2022). These oligosaccharide-based
78 BCPs formed microphase-separated structures easily, which indicates an unusually high potential
79 for microphase separation. In addition, we have revealed that fully bio-based ABA-type triblock
80 copolymers containing maltooligosaccharide as the A block and bio-based poly(δ -decalactone)
81 (PDL; $T_g \approx -60$ °C) as the B block had highly ordered microphase-separated structures and
82 exhibited elastomeric properties, with a stress at break of $\sim 700\%$ and a Young's modulus
83 comparable to that of conventional PS-based TPEs (Isono, Nakahira, et al., 2020). Recently, we
84 replaced unprotected maltooligosaccharide with cellulose triacetate to endow the BCPs with
85 enhanced thermoplasticity. Compared with their amylose triacetate-based counterparts, the cellulose
86 triacetate-based TPEs exhibited a greater self-assembly tendency and superior mechanical
87 performance, likely due to stronger intermolecular interactions (Katsuhara et al., 2021). Because of

88 its inedible nature, the use of cellulose (and its derivatives) can avoid competition with the food
89 supply. Although cellulose-based TPEs have potential as next-generation sustainable TPEs,
90 challenges still exist in controlling and improving the material properties, such as microphase-
91 separated structures, mechanical properties, thermal properties, and biodegradability, for practical
92 applications.

93 An important factor in determining the physical properties of cellulose derivatives is the
94 degree of substitution (DS). For example, good solvents for cellulose acetates depend on the DS.
95 Cellulose triacetate (DS \approx 3) is soluble in dichloromethane and chloroform (CHCl₃) but not in
96 acetone and tetrahydrofuran (THF), whereas cellulose diacetate (DS \approx 2) is soluble in acetone and
97 THF (de Freitas, Senna, & Botaro, 2017). The DS also critically affects the hydrogen bonding
98 profile. Native cellulose (DS = 0) is insoluble in common solvents because of its highly crystalline
99 nature originating from strong inter- and intramolecular hydrogen bonds (Hata & Serizawa, 2021).
100 Free hydroxy groups provide hydrogen bonding sites and increase polarity, which could positively
101 affect the microphase separation and mechanical strength of cellulose acetate-based TPEs. The DS
102 of cellulose acetate is also known to influence biodegradability. Cellulose triacetate does not
103 biodegrade, but cellulose acetates with lower DSs (\sim 2) biodegrade quickly, even in natural
104 environments.(Edgar et al., 2001; Erdal & Hakkarainen, 2022; Kliem, Kreutzbruck, & Bonten,
105 2020; Puls, Wilson, & Hölter, 2011)

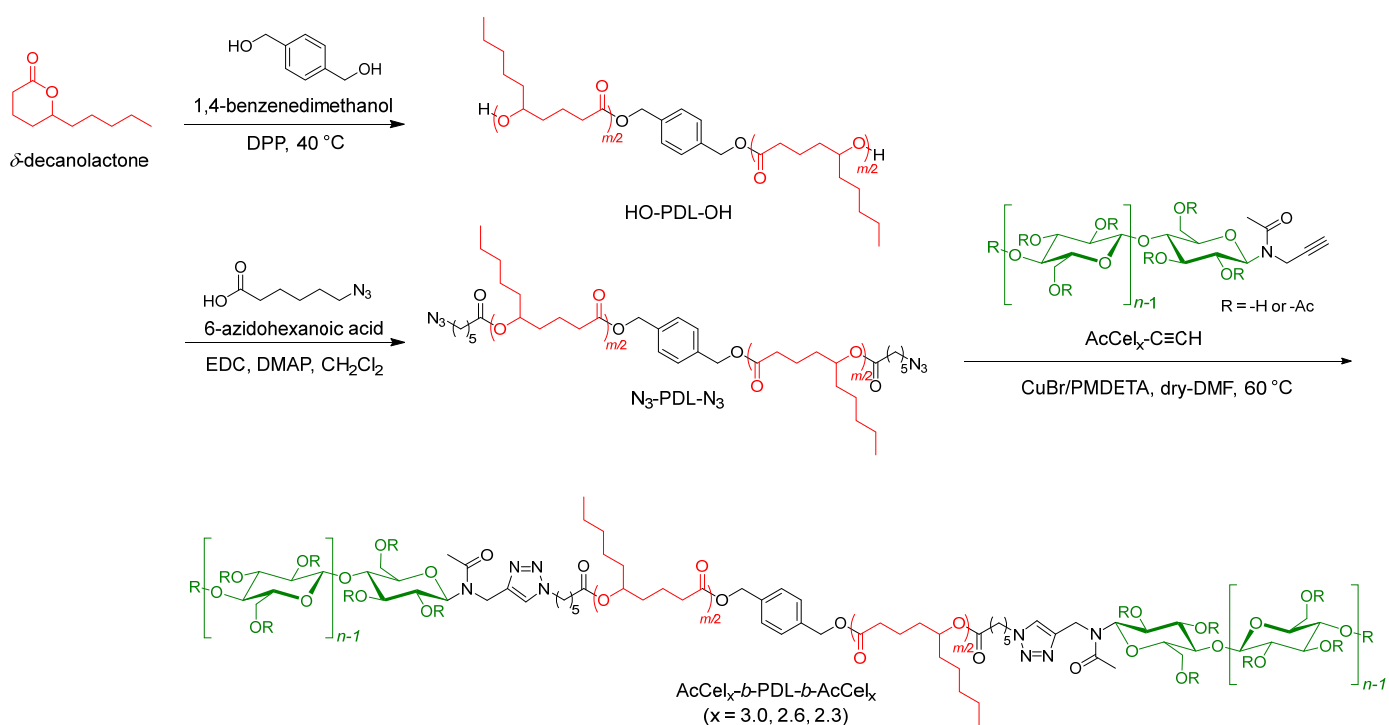
106 Thus, the material properties of cellulose-based TPEs can be improved and optimized by
107 controlling the DS of the cellulose acetate block. In this study, we synthesized cellooligosaccharide
108 acetate-*b*-PDL-*b*-cellooligosaccharide acetate (AcCel_x-*b*-PDL-*b*-AcCel_x, where x is the DS; x = 3.0,
109 2.6, and 2.3) triblock copolymers (**Scheme 1**). Cellooligosaccharide acetate blocks with three
110 different DSs were used to investigate the influence of the DS on the microphase separation
111 behavior and mechanical properties. Small-angle X-ray scattering (SAXS) and atomic force
112 microscopy (AFM) revealed that AcCel_x-*b*-PDL-*b*-AcCel_x tends to form more ordered microphase-
113 separated structures as the DS decreases. Notably, AcCel_{2.6}-*b*-PDL-*b*-AcCel_{2.6} and AcCel_{2.3}-*b*-PDL-

114 *b*-AcCel_{2.3} exhibited superior mechanical properties to AcCel_{3.0}-*b*-PDL-*b*-AcCel_{3.0}. In addition, the
115 biodegradability of AcCel_{*x*}-*b*-PDL-*b*-AcCel_{*x*} in an aqueous environment was enhanced by
116 decreasing the DS of the AcCel_{*x*} segment. The findings of this study reveal that DS is an important
117 factor for governing the properties of cellulose-based BCPs and demonstrate the potential of
118 cellulose-derived TPEs as new sustainable materials.

119

120

Scheme 1. Synthesis of AcCel_{*x*}-*b*-PDL-*b*-AcCel_{*x*}



121

122

123

124

125

126

127

128

129

130

131 2. Experimental section

132 2.1. Materials

133 α -D-Glucose 1-phosphate disodium salt hydrate (α G1P, $\geq 97\%$), 4-(2-hydroxyethyl)-1-
134 piperazineethanesulfonic acid (HEPES, $\geq 99.5\%$, titration), copper(I) bromide (CuBr, 99.999%), and
135 2,5-dihydroxybenzoic acid (98%) were purchased from Sigma Aldrich and used as received.
136 d(+)-cellobiose, sodium sulfate (Na_2SO_4 , $>99.0\%$), anhydrous magnesium sulfate (MgSO_4 , $>95\%$),
137 propargylamine ($>95\%$), acetic anhydride ($>97\%$), hydrochloric acid (HCl, 35–37%), sulfuric acid
138 ($>96.0\%$), ethyl acetate (AcOEt, $>99.3\%$), acetone ($>99.0\%$), *N,N*-dimethylformamide (DMF,
139 $>99.0\%$), *N,N*-dimethylethanamide (DMAc, $>99.0\%$), lithium chloride (LiCl, $>99.0\%$), dry DMF
140 ($>99.5\%$; water content, $<0.001\%$), dry toluene ($>99.5\%$; water content, $<0.001\%$), and dry CH_2Cl_2
141 ($>99.5\%$; water content, $<0.001\%$) were purchased from Kanto Chemical Co., Inc. and used as
142 received. Dichloromethane (CH_2Cl_2 , $>99.0\%$), chloroform (CHCl_3 , $>99.0\%$), and methanol (MeOH,
143 99.6%) were purchased from Junsei Chemical Co., Ltd., and used as received. *N,N,N',N'',N''*-
144 Pentamethyldiethylenetriamine (PMDETA, $>98.0\%$), diphenyl phosphate (DPP, $>98.0\%$), 1,4-
145 benzenedimethanol (BDM, $>99.0\%$), 1-(3-dimethylaminopropyl)-3-ethylcarbodiimide
146 hydrochloride (EDC·HCl, $>98.0\%$), and 4-dimethylaminopyridine (DMAP, $>99.0\%$) were
147 purchased from Tokyo Chemical Industry Co., Ltd. (TCI) and used as received. δ -Decanolactone (δ -
148 DL) was purchased from TCI and purified by distillation over CaH_2 under reduced pressure (6
149 Pa/112 °C). Dowex[®] 50WX2 hydrogen form was purchased from Sigma Aldrich and was washed
150 with MeOH before use. Sucrose phosphorylase (SP) was purchased from Oriental Yeast Co., Ltd.,
151 and kept in a freezer after dissolved in Lysis buffer which composed of 20 mM
152 tris(hydroxymethyl)aminomethane-HCl and 10 mM imidazole. Cellodextrin phosphorylase (CDP)
153 (Hiraishi et al., 2009), 6-azidohexanoic acid (Grandjean et al., 2005), and ethynyl-functionalized
154 cellobiose (CB-C \equiv CH) (Halila, S et al., 2008) were prepared according to previous reported
155 methods.

156

157

158 **2.2. Methods**

159 **¹H NMR measurement.** ¹H NMR (400 MHz) spectra were obtained using a JEOL JNM-ECS 400
160 instrument at 25 °C. Note that ¹H NMR measurement of ethynyl-functionalized
161 cellooligosaccharide (Cel-C≡CH) was performed at 55 °C.

162 **Size exclusion chromatography (SEC).** SEC measurements were performed at 40 °C in THF
163 (flow rate, 1.0 mL min⁻¹) using a Jasco high-performance liquid chromatography system (PU-980
164 Intelligent HPLC Pump, CO-2065 Plus Intelligent Column Oven, RI-2031 Plus Intelligent RI
165 Detector, and DG-2080-53 Degasser) equipped with a Shodex KF-G guard column (4.6 mm × 10
166 mm; particle size, 8 μm) and two Shodex KF-804L columns (linear; particle size 7 μm; 8.0 mm ×
167 300 mm; exclusion limit, 4 × 10⁴). The number-average molecular weight ($M_{n,SEC}$) and dispersity
168 (D) were calculated based on polystyrene standards.

169 **Fourie transform infrared spectroscopy (FT-IR).** The FT-IR spectra were obtained using a
170 PerkinElmer Frontier MIR spectrometer equipped with a single reflection diamond universal
171 attenuated total reflection (ATR) accessory.

172 **Differential scanning calorimetry (DSC) measurement.** The DSC experiments were performed
173 using a Hitachi DSC 7000X under nitrogen atmosphere. All polymer samples were heated to
174 240 °C, cooled to -100 or 30 °C, and heated again to 250 °C at the heating and cooling rate of
175 10 °C min⁻¹.

176 **Thermogravimetric analysis (TGA).** The TGA analysis was performed using Hitachi STA200RV
177 under nitrogen atmosphere. All polymer samples were heated up to 550 °C at the heating rate of
178 10 °C min⁻¹.

179 **Matrix-assisted laser desorption/ionization time-of-flight mass spectrometry (MALDI-TOF**
180 **MS).** The MALDI-TOF MS of the obtained products was performed using a Bruker Daltonick
181 GmbSH Co., Inc. in the reflector mode controlled by the Flexcontrol 3.0 software package. For the
182 Cel-C≡CH, the sample was prepared by mixing an ultrapure water dispersion of the compound (1.0

183 mg mL⁻¹, 200 μL), acetonitrile solution of a matrix (2,5-dihydroxybenzoic acid, 10 mg mL⁻¹, 100
184 μL), and trifluoroacetic acid (0.2% (v/v), 300 μL). A 1 μL aliquot of this mixture was loaded on a
185 sample plate. For ethynyl-functionalized cellooligosaccharide acetate, the ethynyl-functionalized
186 maltooligosaccharide, and ethynyl-functionalized maltooligosaccharide acetate, the samples were
187 prepared by mixing a THF solution of the compound (5 mg mL⁻¹, 100 μL) and a matrix (2,5-
188 dihydroxybenzoic acid, 10 mg mL⁻¹, 500 μL). A 1 μL aliquot of this mixture was loaded was loaded
189 on a sample plate, which was coated by an acetone solution of NaI (1 μL, 1 mmol L⁻¹) as the
190 cationic agent.

191 **Atomic force microscopy (AFM) observation.** The AFM phase images were obtained using a
192 Molecular Imaging PicoPlus atomic force microscope operating in the tapping mode with a silicon
193 cantilever (Nanoworld AG, NANOSENSORSTM PPP-NCH) having resonant frequency and spring
194 constant of 190 kHz and 48 N m⁻¹, respectively. The thin film samples for the AFM observation
195 were prepared by spin-coating (1,500 rpm for 60 s) the polymer solution in CHCl₃ (1 wt%) onto a
196 Si substrate with a native oxide layer.

197 **Scanning electron microscope (SEM).** The samples were mounted on a brass stub put conductive
198 carbon tape and coated gold particle by ion sputtering for 1 min at 15 mA using a Hitachi E-1010.
199 The sample observations were conducted using a JEOL JSM-7001FA scanning electron microscope
200 at an accelerating voltage of 5kV.

201 **Small-angle X-ray scattering (SAXS) and wide-angle X-ray diffraction (WAXD).** The SAXS
202 and WAXD measurements of the obtained polymers were performed at the BL-6A or BL-10C
203 beamline of the Photon Factory in the High Energy Accelerator Research Organization (KEK,
204 Tsukuba, Japan) using X-ray beams with $\lambda = 0.15$ nm at room temperature. The scattering data were
205 collected by a 2D detector (PILATUS3 1M or 2M (SAXS) (Dectris Ltd.); PILATUS3 100K or
206 200K (WAXD) (Dectris Ltd.)), where the samples-to-detector distance was set to be 1.5 m and 0.2
207 m for SAXS and WAXD measurement, respectively. The scattering angle (θ) was calibrated using
208 silver behenate (Nagara Science Co., Ltd) as the standard and derived the scattering vector (q) from

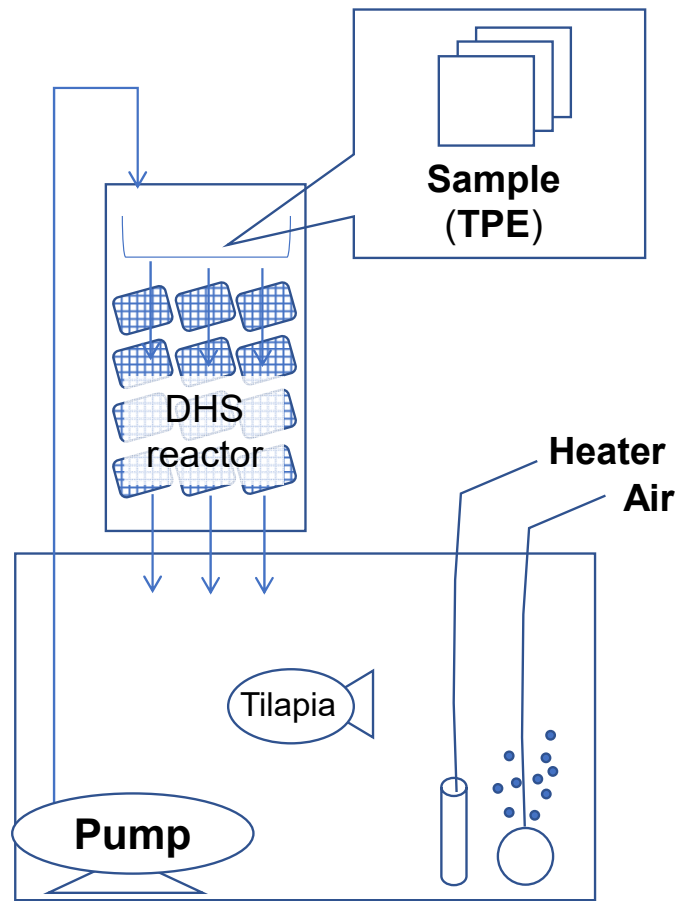
209 Bragg's equation ($|q| = (4\pi/\lambda)\sin(\theta/2)$). The domain-spacing (d) value was calculated by $d = 2\pi/|q^*$
210 ($|q^*$ is principal scattering peak position). The polymer films or powders were sandwiched by two
211 pieces of Kapton tapes with a spacer of a stain less washer, which were applied for the
212 measurement.

213 **Tensile testing.** The tensile tests were performed with an 34SC-1 (INSTRON) tensile tester at the
214 temperature of 20 °C and the humidity of 45%. The film samples for the tensile tests were prepared
215 by casting the polymer solutions from the CHCl₃ (15 mL) on a Teflon dish and drying at r.t. for 2 d
216 followed by vacuum drying at r.t. for 2 d. The obtained elastic films were cut into a dog bone shape
217 of 12 × 2 × ca. 0.13 mm (Japanese Industrial Standards (JIS) K6251). For each film, three samples
218 were tested and the average values of the elastic modulus, strain at break, stress at break, and
219 toughness were calculated. The crosshead speed applied during the measurements was 10 mm
220 min⁻¹. The strain at break was taken as the engineering strain where the stress drops suddenly.

221 **Biodegradation test.** Biodegradation test was conducted in freshwater closed recirculating
222 aquaculture system (RAS) rearing the Nile tilapia *Oreochromis niloticus* where samples cut into 1
223 cm squares were put in polyethylene net (**Fig. 1**). The temperature of 200-L fish tank was controlled
224 at 26 °C by heater. Dissolved oxygen level was maintained at saturation (~8 mg/L) by aeration.

225 To maintain the water quality for rearing fish healthy, a 45-L down hanging sponge (DHS) reactor
226 with the flow rate of 600 L/h by water pump was equipped for nitrification of ammonia nitrogen.
227 Fish density of RAS in this study was approximately 4 kg fish/kL. The 900 CFU/mL bacteria in the
228 water of RAS was detected using culture medium for determining a total viable cell count, Compact
229 dry (Nissui Pharmaceutical Co., Ltd.). Pictures of samples were taken with a digital camera (Floyd
230 4K, Wraymer, Japan) installed on a stereo microscope (SZX10, Olympus, Japan) in once a week.
231 After the biodegradation test, the samples were washed pure water and lyophilized for 1 day.

232



233

234

Fig. 1. Schematic images of the recirculating aquaculture system (RAS) used in this study.

235

236

237

238

239

240

241

242

243

244

245

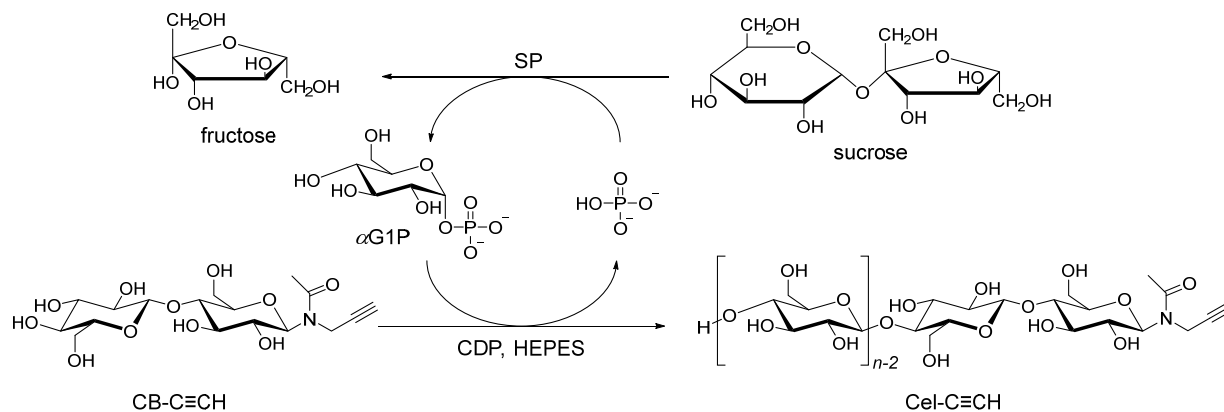
246

247

248 **2.3. Synthesis details**

249 **Synthesis of ethynyl-functionalized cellooligosaccharide (Cel-C≡CH) using CDP and SP**

250 **Scheme 2. Synthesis of Cel-C≡CH**



252 10 mM α G1P, 50 mM CB-C≡CH, and 500 mM sucrose were incubated with 50 $\mu\text{g mL}^{-1}$ CDP and
 253 5 U mL^{-1} SP in 50 mM HEPES buffer solutions (pH 7.5, 104 mL, divided into 11 centrifuge tubes)
 254 at 40 °C. After incubating for 7 days, the reaction mixtures were centrifuged to isolate the insoluble
 255 product and the resulting pellet was washed with water followed by centrifugation at 14,000 rpm for
 256 20 min at 4 °C several times to give swollen Cel-C≡CH. The aliquot of the obtained product was
 257 freeze-dried in vacuo for 2 days to give white powder (6.68 g). Yield: 58.4%.

258 $M_{n,\text{NMR}} = 1,170 \text{ g mol}^{-1}$, $M_{n,\text{MALDI}} = 1,210 \text{ g mol}^{-1}$.

259 $^1\text{H NMR}$ (400 MHz, 10% (w/w) NaOD-D₂O): δ (ppm) 5.59–5.42, 4.55–4.32 (2x m, rotamers 1H,
 260 -CHN(Ac)-), 4.15 (d, $J = 8.0 \text{ Hz}$, 1H $\times (n-1)$, $H-1^{\text{Cel}}$), 4.06–2.67 (m, 9H $\times n + 3\text{H}$, $H-2, -3, -4, -5, -$
 261 $6^{\text{Cel}n}$, $\text{OH}^{\text{Cel}n}$, -N(Ac)CH₂-), 2.53–2.45, 2.32–2.17 (m, rotamers, 1H, -CCH), 1.67–1.55 (m, 3H,
 262 -N(C=O)CH₃).

263

264

265

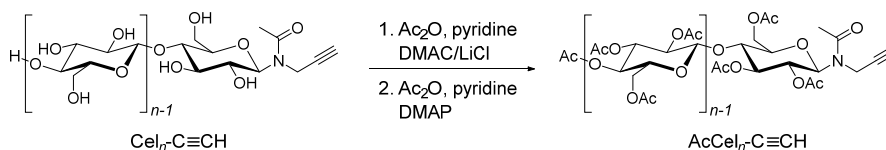
266

267

268

269 **Synthesis of ethynyl-functionalized cellobiosaccharide triacetate (AcCel_{3,0}-C≡CH)**

270 **Scheme 3.** Synthesis of AcCel_{3,0}-C≡CH



271

272 Wet Cel_n-C≡CH (6.28 g, by dry weight) was dispersed in acetone and centrifuged twice (7,000
 273 rpm/30 min/0 °C, 7,000 rpm/15 min/0 °C). The pellet was dispersed in acetone (300 mL) and stirred
 274 over night at room temperature. After the centrifugation (7,000 rpm/15 min/0 °C), the pellet was
 275 washed with DMAc followed by centrifugation (7,000 rpm/15 min/0 °C). The pellet was dispersed
 276 in DMAc (250 mL) and stirred at r.t. After 3 h, LiCl (4.02 g, 94.8 mmol) was added to the mixture
 277 and kept stirring over-night. After adding a solution of acetic anhydride in pyridine (1/1 (v/v), 40
 278 mL), the mixture was stirred 5 d. The reaction mixture was diluted with CH₂Cl₂ and washed with
 279 1M HCl (100 mL) three times. The organic layer was dried over MgSO₄ and concentrated to give a
 280 white solid. The obtained solid and DMAP (139.6 mg, 1.14 mmol) was added to a solution of acetic
 281 anhydride in pyridine (1/2 (v/v), 120 mL) and stirred at r.t. for 3 d. After removing the solvent by
 282 evaporation, the residue was dissolved in ethyl acetate and washed with 1 M HCl and saturated
 283 NaHCO₃ solutions. After the organic layer was dried over Na₂SO₄ and concentrated by evaporation,
 284 the residue was dissolved with a little of CH₂Cl₂ and poured into the cold-MeOH. The precipitated
 285 product was dried under vacuo to give AcCel_{3,0}-C≡CH as a white solid (6.68 g). Yield: 55.7%.

286 $M_{n,\text{NMR}} = 2,080 \text{ g mol}^{-1}$, $M_{n,\text{MALDI}} = 2,360 \text{ g mol}^{-1}$, $M_{n,\text{SEC}} = 2,560 \text{ g mol}^{-1}$ (THF), $D = 1.06$ (THF).

287 ¹H NMR (400 MHz, DMSO-*d*₆): δ (ppm) 6.09 (d), 5.88–5.74 (m) (2x, 1H, rotamers, -CHN(Ac)-),

288 5.53–3.22 (m, 7H × (n-1) + 8H, H-1, -2, -3, -4, -5, -6^{AcCel_n} of anhydro glucose repeating unit and

289 non-reducing terminal end group, -N(Ac)CH₂-), 2.70–2.63 (m, 1H, -CCH), 2.34–1.64 (m, 9n+6,

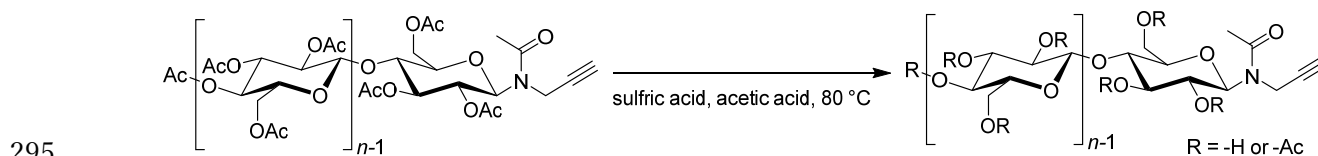
290 CH₃-Ac^{AcCel_n}, -N(C=O)CH₃).

291

292

293 **Deacetylation of AcCel_{3.0}-C≡CH**

294 **Scheme 4. Deacetylation of AcCel_{3.0}-C≡CH**



296 **Synthesis of AcCel_{2.6}-C≡CH**

297 Typical deacetylation procedure is as follows (Method A): AcCel_{3.0}-C≡CH (1.49 g, 645 μmol,

298 $M_{n,MALDI} = 2,310$, $D = 1.07$) was dissolved in acetic acid (25 mL) in a round-bottom flask.

299 Concentrated sulfuric acid (410 μL) was added slowly to the solution followed by water (2.5 mL),

300 and while the mixture was stirred at 80 °C. After 9.5 min, water was added to the mixture to

301 precipitate the product. The precipitate was filtered and washed several times using water. After

302 drying under reduced pressure, the cellooligosaccharide acetate with degree of the substitution (DS)

303 of 2.6 was obtained as a white powder (1.33 g). Note that the DS of cellooligosaccharide acetate

304 was labeled as subscript number, i.e., AcCel_x-C≡CH (x means the DS).

305 Yield: 95.1%

306 See **Fig. S7** for ¹H NMR spectrum.

307

308

309

310

311

312

313

314

315

316

317 **Synthesis of AcCel_{2.3}-C≡CH**

318 The method A was used for the deacetylation of AcCel_{3.0}-C≡CH (1.50 g, 649 μmol,
319 $M_{n,MALDI} = 2,310$, $D = 1.07$) with acetic acid (25 mL), concentrated sulfuric acid (410 μL), and
320 water (2.5 mL) for 20 min to synthesize AcCel_{2.3}-C≡CH with the DS of 2.3 (1.01 g).

321 Yield: 75.1%

322 See **Fig. S7** for ¹H NMR spectrum.

323

324

325

326

327

328

329

330

331

332

333

334

335

336

337

338

339

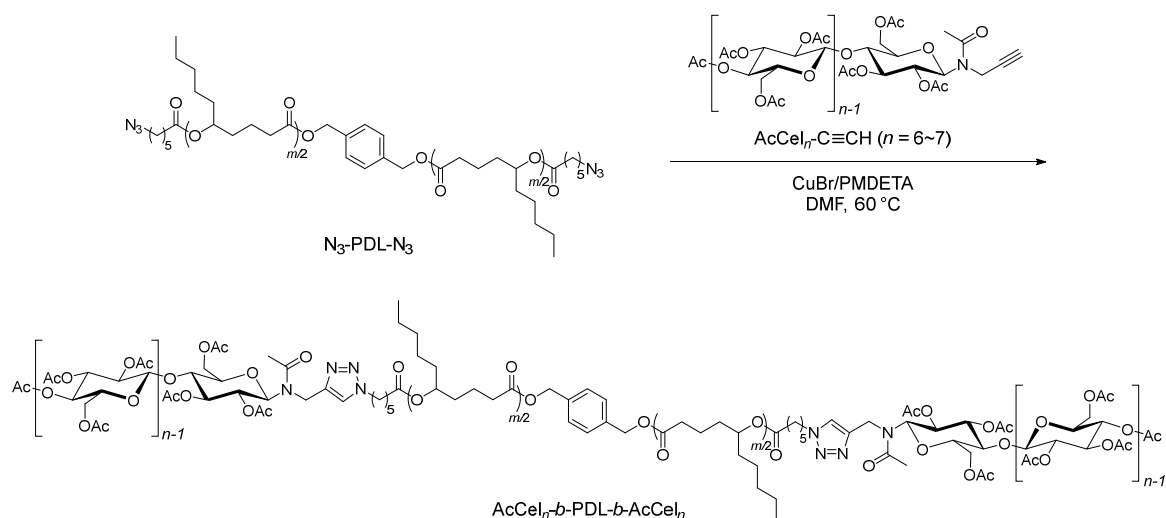
340

341

342

343 **Synthesis of ABA-type BCP consisting of cellooligosaccharide acetate and PDL (AcCel_x-b-**
 344 **PDL-b-AcCel_x) via click reaction**

345 **Scheme 5. Synthesis of AcCel_x-b-PDL-b-AcCel_x**



348 A typical click reaction procedure is as follows (Method B): A degassed solution of N₃-PDL-N₃
 349 ($M_{n,NMR} = 17,800 \text{ g mol}^{-1}$, 1.43 g, 80.3 μmol) and PMDETA (37.8 μL , 181 μmol) in dry DMF (20
 350 mL) was transferred to a Schlenk tube in which AcCel_n-C≡CH (425.1 mg, 184 μmol) and CuBr
 351 (27.7 mg, 193 μmol) were placed. The mixture was stirred for 43 h at 60 °C under an argon
 352 atmosphere. After cooling to room temperature, Dowex[®] 50WX2 and a few drops of water were
 353 added to remove Cu catalyst. The unreacted AcCel_{3,0}-C≡CH was removed by the preparative SEC
 354 in CHCl₃ to give AcCel_{3,0}-b-PDL-b-AcCel_{3,0} as a pale-yellow elastic material (1.18 g). Yield:
 355 65.6%.

356 $M_{n,SEC} = 27,700 \text{ g mol}^{-1}$ (THF), $D = 1.03$ (THF), $M_{n,total} = 22,400 \text{ g mol}^{-1}$.

357 See **Fig. S10** for ¹H NMR spectrum.

358

359

360

361

362

363 **Synthesis of AcCel_{2,6}-*b*-PDL-*b*-AcCel_{2,6}**

364 The Method B was used for the click reaction of N₃-PDL-N₃ ($M_{n,NMR} = 17,800 \text{ g mol}^{-1}$, 1.60 g,
365 89.9 μmol) and AcCel_{*n*}-C \equiv CH (444.6 mg, 204 μmol) in dry DMF (20 mL) with CuBr (28.1 mg,
366 196 μmol) and PMDETA (41.3 μL , 198 μmol) to synthesize AcCel_{2,6}-*b*-PDL-*b*-AcCel_{2,6}. The
367 crude product was purified by reprecipitation to give AcCel_{2,6}-*b*-PDL-*b*-AcCel_{2,6} as a white elastic
368 material (1.19 g). Yield: 59.6%.

369 $M_{n,SEC} = 30,200 \text{ g mol}^{-1}$ (THF), $D = 1.04$ (THF), $M_{n,total} = 22,200 \text{ g mol}^{-1}$.

370 See **Fig. S11** for ¹H NMR spectrum.

371

372 **Synthesis of AcCel_{2,3}-*b*-PDL-*b*-AcCel_{2,3}**

373 The Method B was used for the click reaction of N₃-PDL-N₃ ($M_{n,NMR} = 17,800 \text{ g mol}^{-1}$, 1.40 g,
374 78.7 μmol) and AcCel_{*n*}-C \equiv CH (372.5 mg, 178 μmol) in dry DMF (20 mL) with CuBr (27.0 mg,
375 188 μmol) and PMDETA (37.8 μL , 181 μmol). The crude product was purified by reprecipitation to
376 give AcCel_{2,3}-*b*-PDL-*b*-AcCel_{2,3} as a white elastic material (1.19 g). Yield: 68.8%.

377 $M_{n,SEC} = 26,500 \text{ g mol}^{-1}$ (THF), $D = 1.04$ (THF), $M_{n,total} = 22,000 \text{ g mol}^{-1}$.

378 See **Fig. S12** for ¹H NMR spectrum.

379

380

381

382

383

384

385

386

387

388

389 3. Results and discussion

390 3.1. Cellooligosaccharide preparation

391 We first investigated the improved synthesis of propargyl-functionalized
392 cellooligosaccharide (Cel-C≡CH), a precursor of cellooligosaccharide triacetate, through enzymatic
393 polymerization (**Scheme 2**; Hiraishi et al., 2009; Katsuhara et al., 2021; Kuga, Sunagawa, &
394 Igarashi, 2022; Petrović, Kok, Woortman, Ćirić, & Loos, 2015; Pylkkänen et al., 2020; Serizawa,
395 Kato, Okura, Sawada, & Wada, 2016; Sugiura, Sawada, Tnaka, & Serizawa, 2021; Sugiura, Saito,
396 Sawada, Tanaka, & Serizawa, 2022). In our previous report, we prepared Cel-C≡CH mainly
397 consisting of 6–8-mers through the cellodextrin phosphorylase (CDP)-mediated oligomerization of
398 α -D-glucose-1-phosphate (α G1P) in the presence of *N*-acetyl-propargyl D-(+)-cellobiose as a primer.
399 Cellooligosaccharides with various functional groups at the reducing end and narrow dispersities
400 (D) were easily obtained using CDP-mediated oligomerization. However, low product yields
401 (~20%) were observed (Katsuhara et al., 2021), likely because phosphoric acid was also produced,
402 which promoted the reverse reaction (i.e., phosphorolysis of the cellooligosaccharide). To improve
403 the product yield, we modified the enzyme polymerization system to avoid the accumulation of
404 phosphoric acid. Sucrose and sucrose phosphorylase were added to the previous system (Katsuhara
405 et al., 2021) to simultaneously reuse the generated phosphoric acid and produce α G1P from sucrose
406 (for details, see Supporting Information (SI)). Consequently, the yield of Cel-C≡CH reached ~60%,
407 which is three times greater than that achieved with our previous protocol (~20%). The
408 characterization data for the obtained Cel-C≡CH are shown in **Fig. S1**. The ^1H NMR signals were
409 assigned to the expected structure and a number-averaged degree of polymerization (DP) of 6.59
410 was calculated, which corresponds to a number-averaged molecular weight ($M_{n,\text{NMR}}$) of 1,170 g
411 mol $^{-1}$. Matrix-assisted laser desorption/ionization time-of-flight mass spectrometry (MALDI-TOF
412 MS) analysis revealed two series of repeating peaks separated by 162 Da in the range of 900–1,500
413 Da. The major and minor series of peaks are consistent with the Na $^+$ and K $^+$ adducts, respectively,
414 of Cel-C≡CH comprising 6–8-mers. The number-averaged molecular weight estimated from the

415 MALDI-TOF MS analysis ($M_{n,\text{MALDI}}$) was 1,210 g mol⁻¹, which is similar to the $M_{n,\text{NMR}}$ value
416 (1,170 g mol⁻¹).

417 The fully acetylated propargyl-functionalized cellooligosaccharide (i.e.,
418 cellooligosaccharide triacetate (AcCel_{3.0}-C≡CH)) was prepared according to the established
419 procedure (**Scheme 3**; Kamitakahara, Enomoto, Hasegawa, & Nakatsubo, 2005; Katsuhara et al.,
420 2021). The $M_{n,\text{MALDI}}$ value of the synthesized AcCel_{3.0}-C≡CH (2,310 g mol⁻¹; **Fig. S2**) in this study
421 was slightly larger than that of our previously reported AcCel_{3.0}-C≡CH ($M_{n,\text{MALDI}} = 2,120$ g mol⁻¹;
422 **Fig. S3**). As revealed by MALDI-TOF MS analysis, AcCel_{3.0}-C≡CH synthesized in this work
423 exhibited repeating peaks corresponding to 6–11-mers, whereas our previous sample exhibited
424 repeating peaks corresponding to 6–9-mers (**Fig. S3**) (Katsuhara et al., 2021). This result was
425 further supported by size-exclusion chromatography (SEC) measurements, with the M_n determined
426 by SEC ($M_{n,\text{SEC}}$) for AcCel_{3.0}-C≡CH ($M_{n,\text{SEC}} = 2,560$ g mol⁻¹) synthesized in this study being larger
427 than that of the previous sample ($M_{n,\text{SEC}} = 2,180$ g mol⁻¹) (**Fig. S4**).

428 Next, the partial deacetylation of AcCel_{3.0}-C≡CH was performed in the presence of
429 sulfuric acid to obtain cellooligosaccharide acetates with various DSs (**Scheme 4**; Cerqueira,
430 Valente, Filho, & Burrows, 2009; Kono, Hashimoto, & Shimizu, 2015; Tezuka & Tsuchiya, 1995).
431 We found that the DS could be easily controlled between 3.0 and 2.3 by varying the reaction time.
432 AcCel_{2.6}-C≡CH and AcCel_{2.3}-C≡CH were obtained by hydrolyzing for 9.5 and 20 min, respectively
433 (for details, see the Supporting Information (SI) and **Figs. S5–S7**). The DS of the product was
434 determined by comparing the ¹H NMR signal intensities for the protons of the acetyl groups and
435 glycosidic ring. Importantly, the propargyl group at the reducing end remained intact during
436 deacetylation, as evidenced by the minor ¹H NMR signal of the methylidyne proton at ~2.88 ppm
437 (**Fig. S7a**). In addition, the intensity of the IR absorption band at ~3,500 cm⁻¹ corresponding to
438 hydroxy groups increased when the DS decreased (**Fig. S7b**), which is consistent with the
439 generation of more hydroxy groups as deacetylation proceeds. The MALDI-TOF MS spectra of
440 AcCel_{2.6}-C≡CH and AcCel_{2.3}-C≡CH exhibited a series of repeated peaks that differed by ~42 Da

441 from the signals of AcCel_{3.0}-C≡CH (**Figs. S5** and **S6**), which corresponds to the difference in
442 molecular mass between the acetoxy group (OAc, 59.01 Da) and the hydroxy group (OH, 17.00
443 Da). These results indicate that the deacetylation of AcCel_{3.0}-C≡CH proceeded, while the ethynyl
444 group was maintained. Thus, we successfully synthesized three AcCel_x-C≡CH samples with
445 different DSs but similar M_n and D values ($\sim 2,000$ g mol⁻¹ and 1.07, respectively) (**Fig. S7c**).

447 3.2. BCP synthesis

448 To synthesize the target BCPs (AcCel_{3.0}-*b*-PDL-*b*-AcCel_{3.0}, AcCel_{2.6}-*b*-PDL-*b*-AcCel_{2.6},
449 and AcCel_{2.3}-*b*-PDL-*b*-AcCel_{2.3}), in which the DS of the cellooligosaccharide acetate block varies,
450 an α,ω -diazido-functionalized PDL (N₃-PDL-N₃; $M_{n,NMR} = 17,800$ g mol⁻¹, $D = 1.05$) was
451 synthesized according to our established procedure (Isono, Nakahira, et al., 2020; Isono, Ree,
452 Tajima, Borsali, & Satoh, 2018; Katsuhara et al., 2021) (for details, see the SI, **Schemes S1** and **S2**,
453 and **Figs. S8** and **S9**). A copper-catalyzed azido-alkyne click reaction between N₃-PDL-N₃ and the
454 AcCel_x-C≡CH samples produced the target BCPs in 60–70% isolated yield (**Scheme 5**). After the
455 click reaction, the reaction mixture was treated with a cation exchange resin and then reprecipitated
456 in MeOH to afford the BCP. However, in the case of AcCel_{3.0}-*b*-PDL-*b*-AcCel_{3.0}, unreacted
457 AcCel_{3.0}-C≡CH could not be removed by reprecipitation because of its poor solubility in MeOH.
458 As we were unable to find a solvent that selectively dissolved AcCel_{3.0}-C≡CH while precipitating
459 BCP, unreacted AcCel_{3.0}-C≡CH was removed by preparative SEC, which afforded AcCel_{3.0}-*b*-PDL-
460 *b*-AcCel_{3.0} in 65.6% yield. In contrast, unreacted AcCel_{2.6}-C≡CH and AcCel_{2.3}-C≡CH were easily
461 removed by simple reprecipitation in MeOH, giving AcCel_{2.6}-*b*-PDL-*b*-AcCel_{2.6} and AcCel_{2.3}-*b*-
462 PDL-*b*-AcCel_{2.3} in 95.1% and 75.1% yield, respectively. This behavior suggests that the reduced
463 DSs of AcCel_{2.6}-C≡CH and AcCel_{2.3}-C≡CH impart improved solubility in polar solvents such as
464 MeOH.

465 FT-IR spectroscopy confirmed that each click reaction proceeded quantitatively, as the
466 absorption band at $\sim 2,100$ cm⁻¹ derived from azido groups disappeared completely. The ¹H NMR

467 spectra of the products exhibited proton signals corresponding to AcCel_x (5.4–3.0 ppm) and PDL
 468 moieties (5.0–4.7, 2.6–0.7 ppm) as well as triazole rings (~7.4 and 7.3 ppm) (**Figs. S10–12**).
 469 Moreover, SEC elution peaks appeared at higher molecular weights than for N₃–PDL–N₃ while
 470 maintaining a unimodal shape, and no elution peak corresponding to unreacted AcCel_x–C≡CH was
 471 observed (**Fig. S13**). Collectively, these results support the successful synthesis of the target BCPs.
 472 The detailed characteristics (molecular weight, *D*, volume fraction of PDL segments (*f*_{PDL})) of
 473 AcCel_{3.0}-*b*-PDL-*b*-AcCel_{3.0}, AcCel_{2.6}-*b*-PDL-*b*-AcCel_{2.6}, and AcCel_{2.3}-*b*-PDL-*b*-AcCel_{2.3} are
 474 summarized in **Table 1**.

475

476 **Table 1.** Molecular characteristics of AcCel_x-*b*-PDL-*b*-AcCel_x

Polymer	<i>M</i> _n	<i>M</i> _{n,SEC} ^e	<i>D</i> ^e	<i>T</i> _{g,PDL} ^f [°C]	<i>T</i> _{g,AcCel} ^f [°C]	<i>f</i> _{PDL} ^h
AcCel _{3.0} –C≡CH	2,310 ^a	2,560	1.06	-	110	-
AcCel _{2.6} –C≡CH	2,180 ^b	2,590	1.06	-	116	-
AcCel _{2.3} –C≡CH	2,090 ^b	2,590	1.06	-	121	-
N ₃ –PDL–N ₃	17,800 ^c	22,000	1.04	-58	-	-
AcCel _{3.0} - <i>b</i> -PDL- <i>b</i> -AcCel _{3.0}	22,400 ^d	27,700	1.03	-55	n.d. ^g	0.79
AcCel _{2.6} - <i>b</i> -PDL- <i>b</i> -AcCel _{2.6}	22,200 ^d	28,400	1.04	-56	n.d. ^g	0.80
AcCel _{2.3} - <i>b</i> -PDL- <i>b</i> -AcCel _{2.3}	22,000 ^d	27,600	1.04	-57	n.d. ^g	0.81

477 ^aDetermined by MALDI-TOF MS. ^bCalculated as *M*_n of AcCel_{3.0}–C≡CH – (3 – DS) × (*M*_n of an
 478 acetyl group (43.05) – atomic weight of H (1.01)) × DP. ^cDetermined by ¹H NMR spectroscopy in
 479 CDCl₃. ^dCalculated from the *M*_n values AcCel_x–C≡CH and N₃–PDL–N₃. ^eDetermined by SEC in
 480 THF using PS standards. ^fDetermined using DSC at a heating rate of 10 °C min⁻¹. ^gNot determined.
 481 ^hCalculated using the density of each block: 1.29 g cm⁻³ for AcCel_x–C≡CH and 0.97 g cm⁻³ for
 482 PDL.

483

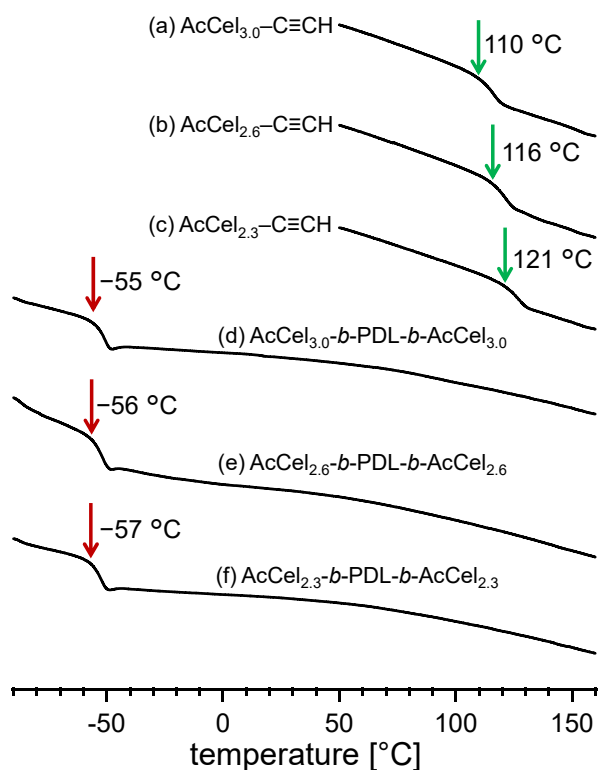
484 3.3. Thermal properties

485 Thermal properties, such as the *T*_g and degradation temperature, are critical characteristics
 486 for elastomer applications. Thus, we investigated the thermal properties of the AcCel_x-*b*-PDL-*b*-
 487 AcCel_x samples and their constituent blocks using differential scanning calorimetry (DSC) and
 488 thermogravimetric analysis (TGA) under a N₂ atmosphere. DSC analysis of AcCel_x–C≡CH with
 489 different DSs revealed an increase in *T*_g (*T*_{g,AcCel}) with decreasing DS (110, 116, and 121 °C for DS
 490 = 3.0, 2.6, and 2.3; **Figs. 2a–c**). This behavior is attributed to an increase in molecular interactions
 491 through hydrogen bonding as DS decreases, which results in decreased chain mobility (Kamide &

492 Saitohal, 1985). The DSC curves of $\text{AcCel}_x\text{-}b\text{-PDL-}b\text{-AcCel}_x$ during the second heating process
493 exhibited a baseline shift at approximately $-55\text{ }^\circ\text{C}$ corresponding to the T_g of the PDL segment
494 ($T_{g,\text{PDL}}$; **Figs. 2d–f** and **S14**). The T_g of AcCel_x ($T_{g,\text{AcCel}}$) was not clearly observed because of the
495 small volume fraction of this segment in the BCPs ($f_{\text{AcCel}_x} \approx 0.2$).

496 TGA analysis revealed a 5% weight-loss temperature ($T_{d5\%}$) of $\sim 300\text{ }^\circ\text{C}$ for the synthesized
497 BCPs, $\text{AcCel}_x\text{-C}\equiv\text{CH}$, and $\text{N}_3\text{-PDL-}\text{N}_3$, which ensures sufficient thermal stability (**Figs. S15** and
498 **S16**). Notably, during heating, the BCP films and $\text{AcCel}_x\text{-C}\equiv\text{CH}$ powders underwent a solid–liquid
499 transformation at $160\text{--}200\text{ }^\circ\text{C}$ (**Fig. S16**), indicating that the BCPs are thermoplastic in nature,
500 which is favorable for potential TPE applications.

501



502

503 **Fig. 2.** DSC curves of (a) $\text{AcCel}_{3.0}\text{-C}\equiv\text{CH}$, (b) $\text{AcCel}_{2.6}\text{-C}\equiv\text{CH}$, (c) $\text{AcCel}_{2.3}\text{-C}\equiv\text{CH}$, (d) $\text{AcCel}_{3.0}\text{-}b\text{-}$
504 $\text{PDL-}b\text{-AcCel}_{3.0}$, (e) $\text{AcCel}_{2.6}\text{-}b\text{-PDL-}b\text{-AcCel}_{2.6}$, and (f) $\text{AcCel}_{2.3}\text{-}b\text{-PDL-}b\text{-AcCel}_{2.3}$ during the
505 second heating process.

506

507 3.4. Microphase separation

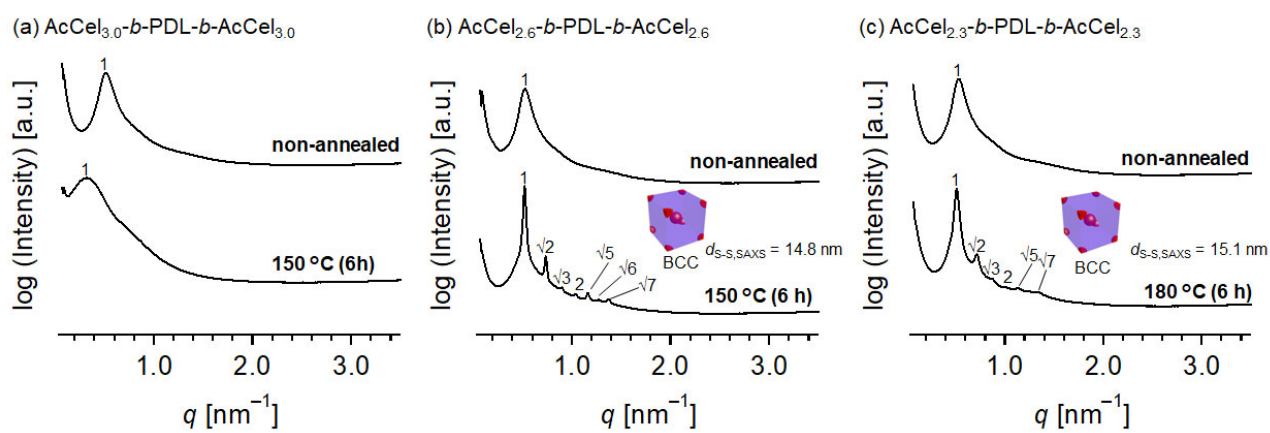
508 Microphase-separated structures are known to affect the mechanical properties of TPEs.
509 Therefore, SAXS measurements were performed to clarify the nanostructures of AcCel_x-*b*-PDL-*b*-
510 AcCel_x in the bulk state. Bulk film samples were prepared by solvent casting from a CHCl₃
511 solution, drying at atmospheric pressure for 2 days, and then vacuum drying at room temperature
512 for 2 days. Subsequently, the films of AcCel_{3.0}-*b*-PDL-*b*-AcCel_{3.0} and AcCel_{2.6}-*b*-PDL-*b*-AcCel_{2.6}
513 were thermally annealed at 150 °C for 6 h under vacuum. On the other hand, the film of AcCel_{2.3}-*b*-
514 PDL-*b*-AcCel_{2.3} was annealed at 180 °C for 6 h because the T_g of AcCel_{2.3}-C≡CH was a little
515 higher than that of AcCel_{3.0}-C≡CH and AcCel_{2.6}-C≡CH. The SAXS profiles of the AcCel_x-*b*-PDL-
516 *b*-AcCel_x films without thermal annealing exhibited only a primary scattering peak, implying ill-
517 defined nanostructures (**Fig. 3**).

518 AcCel_{3.0}-*b*-PDL-*b*-AcCel_{3.0} did not form ordered microphase-separated structures, even
519 after thermal annealing, as indicated by the sole primary scattering peak in the SAXS profile. In
520 contrast, the wide-angle X-ray diffraction (WAXD) profile of annealed AcCel_{3.0}-*b*-PDL-*b*-AcCel_{3.0}
521 showed sharp scattering peaks assignable to cellulose triacetate I crystals (**Fig. S17**). Initially, we
522 expected that AcCel_{3.0}-*b*-PDL-*b*-AcCel_{3.0} would have an ordered body-centered cubic (BCC)
523 spherical morphology, as observed previously for a BCP with a comparable composition and
524 molecular weight (Katsuhara et al., 2021). However, the M_n of the AcCel_{3.0} segment in the present
525 AcCel_{3.0}-*b*-PDL-*b*-AcCel_{3.0} was slightly higher than that in the previous BCP, which greatly
526 affected the crystallization ability, as evidenced by the WAXD analysis of AcCel_{3.0}-C≡CH (**Fig.**
527 **S18**). The nanostructures of semicrystalline BCPs are known to be influenced by the interplay
528 between the driving forces for crystallization and microphase separation (He & Xu, 2012). The
529 strong tendency of AcCel_{3.0}-C≡CH to crystallize owing to its higher M_n could interfere with
530 microphase separation, resulting in the ill-defined nanostructures observed for AcCel_{3.0}-*b*-PDL-*b*-
531 AcCel_{3.0}. Considering the large effect of M_n on the crystallization ability of AcCel_{3.0}, this unique
532 phenomenon requires further investigation in the future.

533 The SAXS profiles of the annealed AcCel_{2.6}-*b*-PDL-*b*-AcCel_{2.6} and AcCel_{2.3}-*b*-PDL-*b*-
534 AcCel_{2.3} films exhibited multiple scattering peaks assignable to BCC spherical structures, whereas
535 the WAXD profiles showed only amorphous halos. The intersphere distances ($d_{S-S,SAXS}$) of AcCel_{2.6}-
536 *b*-PDL-*b*-AcCel_{2.6} and AcCel_{2.3}-*b*-PDL-*b*-AcCel_{2.3} were calculated to be 14.8 and 15.1 nm,
537 respectively ($d_{S-S,SAXS} = (2\pi/q^*)(3/2)^{1/2}$), where the q^* is the primary scattering peak position).
538 Interestingly, AcCel_{2.6}-*b*-PDL-*b*-AcCel_{2.6} and AcCel_{2.3}-*b*-PDL-*b*-AcCel_{2.3} exhibited different d
539 values despite their comparable molecular weights and volume fractions. The d value of a
540 microphase-separated structure is known to reflect the Flory–Huggins interaction parameter (χ), as
541 follows:(Zhou, Janes, Kim, Willson, & Ellison, 2016)
542 $d = a\chi^{1/6}N^{2/3}$ (1)
543 where a is a constant related to the statistical chain length. Eq. (1) demonstrates that d increases
544 with χ . Assuming that AcCel_{2.6}-*b*-PDL-*b*-AcCel_{2.6} and AcCel_{2.3}-*b*-PDL-*b*-AcCel_{2.3} have the same a
545 and N values, a $\chi_{AcCel_{2.3}}/\chi_{AcCel_{2.6}}$ value of 1.13 can be determined based on eq. (1) and the $d_{S-S,SAXS}$
546 values of AcCel_{2.3}-*b*-PDL-*b*-AcCel_{2.3} (15.1 nm) and AcCel_{2.6}-*b*-PDL-*b*-AcCel_{2.6} (14.8 nm). This
547 result indicates that reducing the DS of the AcCel_x segments increases the χ value, leading to
548 ordered microphase-separated structures.

549 AFM was used to visualize the microphase-separated structures in the AcCel_x-*b*-PDL-*b*-
550 AcCel_x thin films (**Fig. 4**). Thin film samples were prepared by spin-coating a CHCl₃ solution (1
551 wt%) of AcCel_x-*b*-PDL-*b*-AcCel_x on bare Si substrates. The AFM phase images of AcCel_x-*b*-PDL-
552 *b*-AcCel_x before thermal annealing exhibited ill-ordered dotted patterns, consistent with the
553 observation of a single primary scattering peak in the SAXS profiles of the non-annealed BCPs.
554 Interestingly, the AFM image of the AcCel_{3.0}-*b*-PDL-*b*-AcCel_{3.0} thin film showed fiber-like
555 structures after thermal annealing, which could be related to the high crystallinity of the AcCel_{3.0}
556 segment. Few such fiber-like structures were observed in the previously synthesized AcCel_{3.0}-*b*-
557 PDL-*b*-AcCel_{3.0} with a comparable composition (Katsuhara et al., 2021). This result indicates that
558 the driving force for crystallization was stronger than that for microphase separation in the present

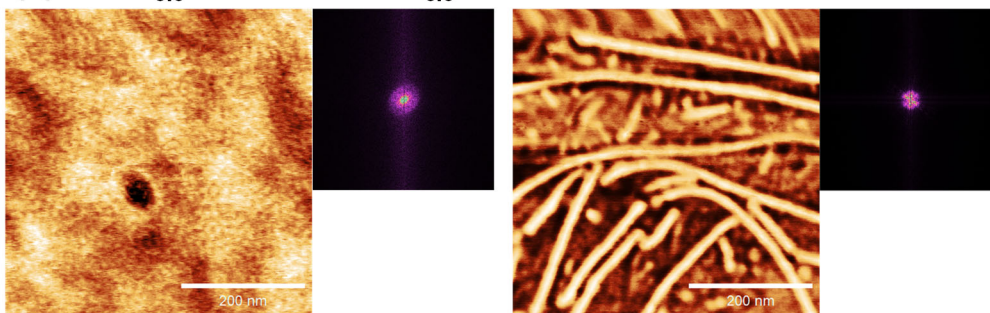
559 AcCel_{3.0}-C≡CH sample with a higher M_n , resulting in the formation of an ill-ordered fiber-like
 560 pattern rather than an ordered microphase-separated structure. In contrast, the AFM phase images of
 561 the thermally annealed AcCel_{2.6}-*b*-PDL-*b*-AcCel_{2.6} and AcCel_{2.3}-*b*-PDL-*b*-AcCel_{2.3} thin films
 562 exhibited highly ordered dotted patterns, reflecting a BCC structure. The intersphere distances
 563 calculated from the fast Fourier transform (FFT) images ($d_{S-S,AFM}$) of the AcCel_{2.6}-*b*-PDL-*b*-
 564 AcCel_{2.6} and AcCel_{2.3}-*b*-PDL-*b*-AcCel_{2.3} films were 13.0 and 13.1 nm, respectively, which are
 565 similar to the $d_{S-S,SAXS}$ values.



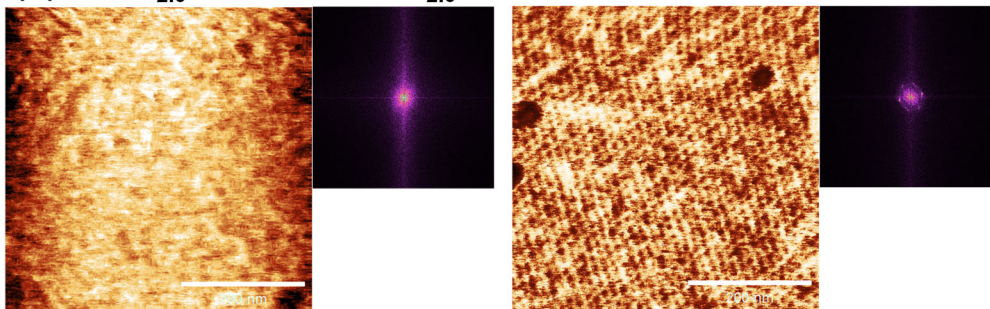
566

567 **Fig. 3.** SAXS profiles of (a) AcCel_{3.0}-*b*-PDL-*b*-AcCel_{3.0}, (b) AcCel_{2.6}-*b*-PDL-*b*-AcCel_{2.6}, and (c)
 568 AcCel_{2.3}-*b*-PDL-*b*-AcCel_{2.3} without thermal annealing (upper) and after thermal annealing at 150 or
 569 180 °C for 6 h (lower).

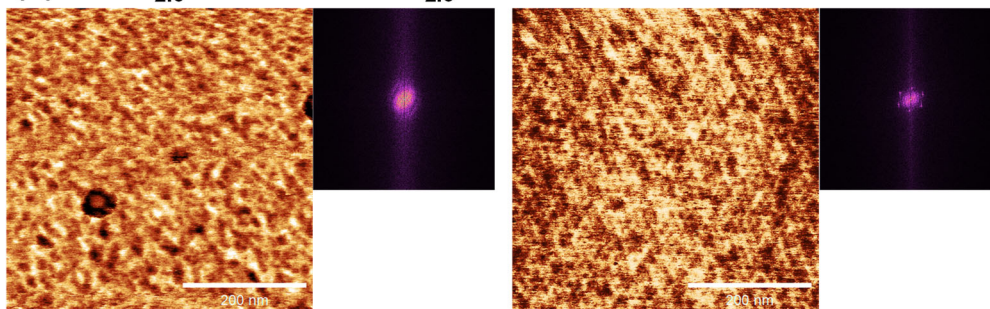
(a) $\text{AcCel}_{3.0}\text{-}b\text{-PDL-}b\text{-AcCel}_{3.0}$



(b) $\text{AcCel}_{2.6}\text{-}b\text{-PDL-}b\text{-AcCel}_{2.6}$



(c) $\text{AcCel}_{2.3}\text{-}b\text{-PDL-}b\text{-AcCel}_{2.3}$



570

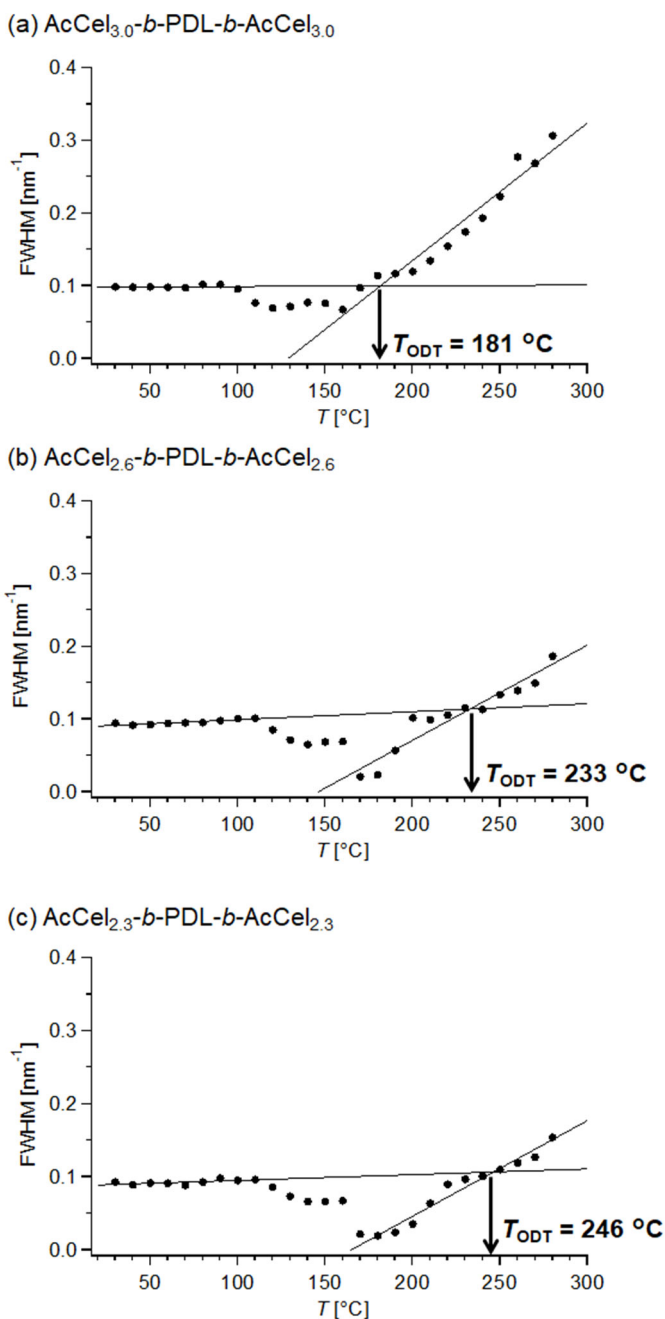
571 **Fig. 4.** AFM phase images of (a) $\text{AcCel}_{3.0}\text{-}b\text{-PDL-}b\text{-AcCel}_{3.0}$, (b) $\text{AcCel}_{2.6}\text{-}b\text{-PDL-}b\text{-AcCel}_{2.6}$, and
572 (c) $\text{AcCel}_{2.3}\text{-}b\text{-PDL-}b\text{-AcCel}_{2.3}$ thin films before (left) and after (right) thermal annealing at 150 °C
573 ($\text{AcCel}_{3.0}\text{-}b\text{-PDL-}b\text{-AcCel}_{3.0}$ and $\text{AcCel}_{2.6}\text{-}b\text{-PDL-}b\text{-AcCel}_{2.6}$) or 180 °C ($\text{AcCel}_{2.3}\text{-}b\text{-PDL-}b\text{-}$
574 $\text{AcCel}_{2.3}$) for 6 h. The insets show the corresponding FFT profiles. Scale bars are 200 nm.

575

576 In situ SAXS measurements were performed during heating to elucidate the order–disorder
577 temperature (T_{ODT}) (**Fig. S19**). The SAXS profiles were acquired at 10 °C steps upon heating from
578 30 to 280 °C. The primary scattering peak of each sample became sharper as the temperature
579 increased to ~170 °C and then broadened at higher temperatures. Importantly, multiple scattering
580 peaks attributed to BCC structures were observed at temperatures of 170–190 and 170–210 °C in

581 the SAXS profiles of AcCel_{2.6}-*b*-PDL-*b*-AcCel_{2.6} and AcCel_{2.3}-*b*-PDL-*b*-AcCel_{2.3}, respectively. This
582 behavior suggested that the mobility of the polymer chains increased up to a certain temperature,
583 which induced microphase separation. Notably, the SAXS profile of AcCel_{3.0}-*b*-PDL-*b*-AcCel_{3.0}
584 also exhibited multiple scattering peaks attributed to BCC structures at 150–160 °C. This would be
585 because the crystallization does not occur at these temperatures. Thus, AcCel_{3.0}-*b*-PDL-*b*-AcCel_{3.0}
586 has sufficient potential for microphase separation in this temperature range, where the AcCel_{3.0}
587 segment does not crystallize; nevertheless, the driving force for crystallization overwhelms that for
588 microphase separation as the temperature decreases, resulting in the formation an ill-ordered fiber
589 structure. Consequently, an ordered microphase-separated structure was not observed in the SAXS
590 profile of AcCel_{3.0}-*b*-PDL-*b*-AcCel_{3.0} at room temperature.

591 The full width at half maximum (FWHM) of the primary scattering peak was plotted
592 against the measurement temperature, and the T_{ODT} was determined as the temperature at which a
593 change in the slope was observed (**Fig. 5**). The T_{ODT} of AcCel_{3.0}-*b*-PDL-*b*-AcCel_{3.0}, AcCel_{2.6}-*b*-
594 PDL-*b*-AcCel_{2.6}, and AcCel_{2.3}-*b*-PDL-*b*-AcCel_{2.3} were estimated to be 181, 233, and 246 °C,
595 respectively. Considering the comparable N and f_{PDL} values of the three BCPs, the increase in T_{ODT}
596 as the DS of the AcCel_x segment decreased indicates a corresponding increase in the χ value (Bates
597 & Fredrickson, 1990). This hypothesis is supported by the observation that AcCel_{2.6}-*b*-PDL-*b*-
598 AcCel_{2.6} and AcCel_{2.3}-*b*-PDL-*b*-AcCel_{2.3} are more likely to form microphase-separated structures
599 than AcCel_{3.0}-*b*-PDL-*b*-AcCel_{3.0}. The increase in the χ value was attributed to the enhanced
600 hydrophilicity of the cellulosic block, which increased the repulsion with the hydrophobic PDL
601 block. Enhanced intrablock interactions via hydrogen bonding between the hydroxy groups on the
602 cellulosic block could also contribute to an increase in χ with decreasing DS. Several previous
603 studies have proposed that the χ value can be increased by enhancing intrablock interactions in
604 typical AB-diblock BCPs (Yoshida et al., 2018; Zhou et al., 2016). Overall, the SAXS and AFM
605 results indicate that the microphase separation behavior of cellulooligosaccharide acetate-based
606 BCPs in both the bulk and thin film states can be controlled by adjusting the DS.



607

608 **Fig. 5.** Dependence of the FWHM of the primary scattering peak on the measurement temperature
 609 for (a) $\text{AcCel}_{3.0}\text{-}b\text{-PDL-}b\text{-AcCel}_{3.0}$, (b) $\text{AcCel}_{2.6}\text{-}b\text{-PDL-}b\text{-AcCel}_{2.6}$, and (c) $\text{AcCel}_{2.3}\text{-}b\text{-PDL-}b\text{-}$
 610 $\text{AcCel}_{2.3}$.

611

612 *3.5. Mechanical properties*

613 Tensile tests were conducted to evaluate the potential of $\text{AcCel}_x\text{-}b\text{-PDL-}b\text{-AcCel}_x$ as
 614 elastomeric materials. The film samples for the tensile tests were prepared using the same procedure
 615 as for the SAXS measurements and then cut into dog-bone shapes. The stress–strain curves are

616 shown in **Fig. 6** and the key mechanical properties (Young's modulus (E), strain at break (ϵ_b), stress
617 at break (σ_b), and toughness) are summarized in **Table 2**. The stress–strain curves of AcCel_x-*b*-PDL-
618 *b*-AcCel_x did not show a yield point, regardless of the annealing history, indicating that these
619 samples have elastomeric properties (**Fig. 6**). In addition, for tensile tests with 10 loading/unloading
620 cycles, all the samples showed a small hysteresis loop, which further supported their sufficient
621 elastic recovery (**Fig. S20**).

622 The σ_b values of non-annealed AcCel_{2.6}-*b*-PDL-*b*-AcCel_{2.6} (2.68 ± 0.08 MPa) and AcCel_{2.3}-
623 *b*-PDL-*b*-AcCel_{2.3} (2.14 ± 0.01 MPa) were slightly higher than that of AcCel_{3.0}-*b*-PDL-*b*-AcCel_{3.0}
624 (1.94 ± 0.13 MPa). Similarly, the ϵ_b values of non-annealed AcCel_{2.6}-*b*-PDL-*b*-AcCel_{2.6} ($420 \pm$
625 15%) and AcCel_{2.3}-*b*-PDL-*b*-AcCel_{2.3} ($378 \pm 7\%$) were 1.2–1.3 times larger than that of AcCel_{3.0}-*b*-
626 PDL-*b*-AcCel_{3.0} ($320 \pm 5\%$). The same trend was observed for the annealed samples, with the ϵ_b
627 values of $192 \pm 5\%$, $310 \pm 10\%$, and $317 \pm 10\%$ for AcCel_{3.0}-*b*-PDL-*b*-AcCel_{3.0}, AcCel_{2.6}-*b*-PDL-*b*-
628 AcCel_{2.6}, and AcCel_{2.3}-*b*-PDL-*b*-AcCel_{2.3}, respectively. These results indicate that reducing the DS
629 effectively improves the mechanical properties of AcCel_x-*b*-PDL-*b*-AcCel_x.

630 Interestingly, the E value of annealed AcCel_{3.0}-*b*-PDL-*b*-AcCel_{3.0} (4.93 ± 0.07 MPa) was
631 three times larger than that of non-annealed AcCel_{3.0}-*b*-PDL-*b*-AcCel_{3.0} (1.64 ± 0.07 MPa), whereas
632 the E values of AcCel_{2.6}-*b*-PDL-*b*-AcCel_{2.6} (1.5 – 1.6 MPa) and AcCel_{2.3}-*b*-PDL-*b*-AcCel_{2.3} (1.2 – 1.4
633 MPa) were not significantly affected by thermal annealing. This difference could be due to the high
634 crystallinity of the annealed AcCel_{3.0} segment. Indeed, for some BCP systems, it has been reported
635 that enhanced crystallinity increases the modulus, although ϵ_b decreases (Jauzein, Huneault, &
636 Heuzey, 2017; Sarasua, Arraiza, Balderdi, & Maiza, 2005; Watts & Hillmyer, 2019). Furthermore,
637 the fiber-like structure observed in annealed AcCel_{3.0}-*b*-PDL-*b*-AcCel_{3.0} could also be an important
638 factor, as such a continuous hard domain would increase the E value. We previously found that a
639 carbohydrate-based elastomer with a hexagonal cylinder (HEX) structure had a higher modulus than
640 an elastomer with a BCC structure (Isono, Nakahira, et al., 2020). This difference originated from
641 the continuous hard domain in the HEX structure, which could bear deformation under stretching

642 (Crawford & Sita, 2015).

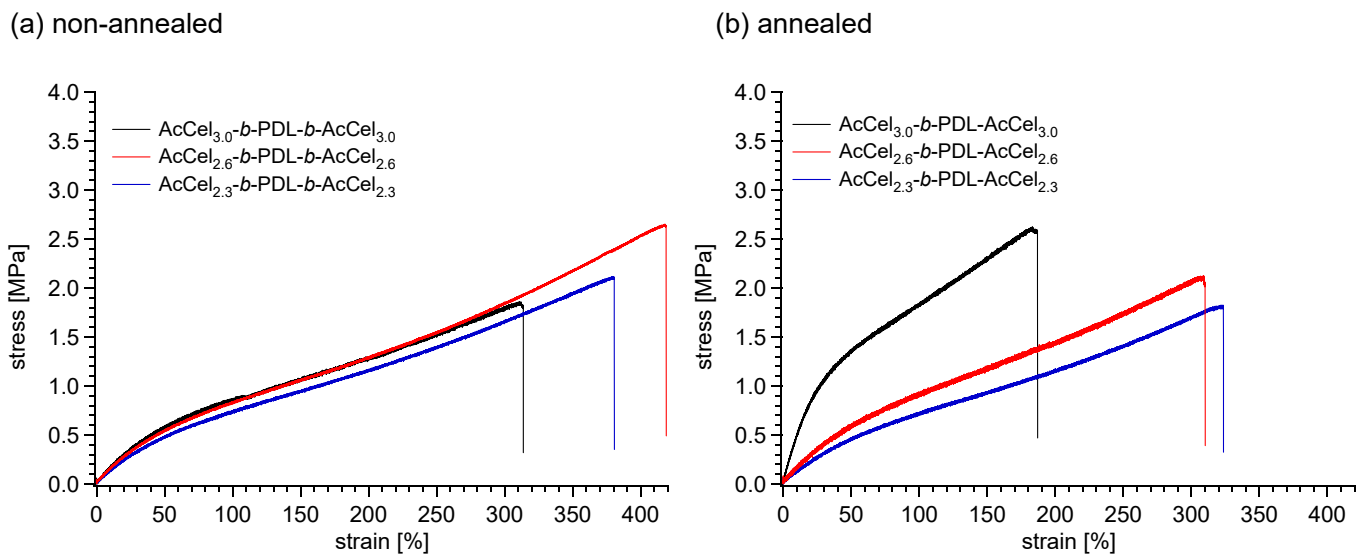
643

644 **Table 2.** Tensile properties of AcCel_x-*b*-PDL-*b*-AcCel_x

BCP	Annealing	E^a [MPa]	ε_b^a [%]	σ_b^a [MPa]	Toughness ^a [MPa]
AcCel _{3.0} - <i>b</i> -PDL- <i>b</i> -AcCel _{3.0}	none	1.64 ± 0.07	320 ± 5	1.94 ± 0.13	3.68 ± 0.27
	150 °C for 6 h	4.93 ± 0.07	192 ± 5	2.63 ± 0.06	3.28 ± 0.13
AcCel _{2.6} - <i>b</i> -PDL- <i>b</i> -AcCel _{2.6}	none	1.53 ± 0.03	420 ± 15	2.68 ± 0.08	5.89 ± 0.38
	150 °C for 6 h	1.56 ± 0.10	310 ± 10	2.15 ± 0.10	3.67 ± 0.24
AcCel _{2.3} - <i>b</i> -PDL- <i>b</i> -AcCel _{2.3}	none	1.38 ± 0.06	378 ± 7	2.14 ± 0.01	4.35 ± 0.13
	180 °C for 6 h	1.23 ± 0.04	317 ± 10	1.80 ± 0.10	3.11 ± 0.28

645 ^aTensile properties are shown as average values (with standard deviations) for three specimens.

646



647

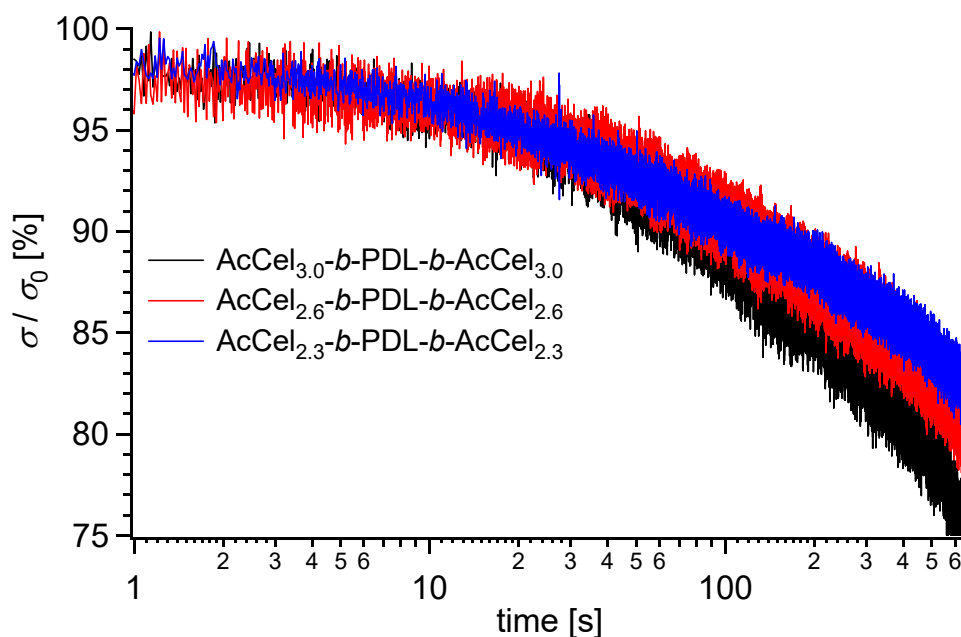
648 **Fig. 6.** Typical stress–strain curves of AcCel_{3.0}-*b*-PDL-*b*-AcCel_{3.0} (black), AcCel_{2.6}-*b*-PDL-*b*-
649 AcCel_{2.6} (red), and AcCel_{2.3}-*b*-PDL-*b*-AcCel_{2.3} (blue) (a) before and (b) after thermal annealing.

650

651 Furthermore, we investigated the stress relaxation behavior to evaluate the impact of DS on
652 material deformation. Stress relaxation experiments were performed by monitoring the stress
653 response of a sample under a constant applied strain of 70%. The average slope in the range of 30–
654 300 s in the semi-log stress relaxation curve is smaller for AcCel_{3.0}-*b*-PDL-*b*-AcCel_{3.0} (–11.5) than
655 for AcCel_{2.6}-*b*-PDL-*b*-AcCel_{2.6} (–9.04) and AcCel_{2.3}-*b*-PDL-*b*-AcCel_{2.3} (–8.48), indicating that
656 stress relaxation was suppressed as DS decreased (**Fig. 7**). The stronger intermolecular forces

657 derived from hydrogen bonding in the AcCel_{2.6} and AcCel_{2.3} segments likely prevented chain
 658 pullout and suppressed stress relaxation. Elastomers bearing hydrogen bonding motifs on their hard
 659 segments have been found to exhibit less stress relaxation than those without hydrogen
 660 bonds.(Watts & Hillmyer, 2019) This stronger hydrogen bonding also improves the mechanical
 661 properties, such as σ_b and ϵ_b . In addition, the higher potential of AcCel_{2.6}-*b*-PDL-*b*-AcCel_{2.6} and
 662 AcCel_{2.3}-*b*-PDL-*b*-AcCel_{2.3} to form ordered microphase-separated structures could decrease stress
 663 relaxation by increasing the energy required for chain pullout.(Watts & Hillmyer, 2019) Overall, the
 664 tensile and stress relaxation tests reveal that the DS is a highly important factor for controlling the
 665 mechanical properties of cellulose-based elastomers.

666



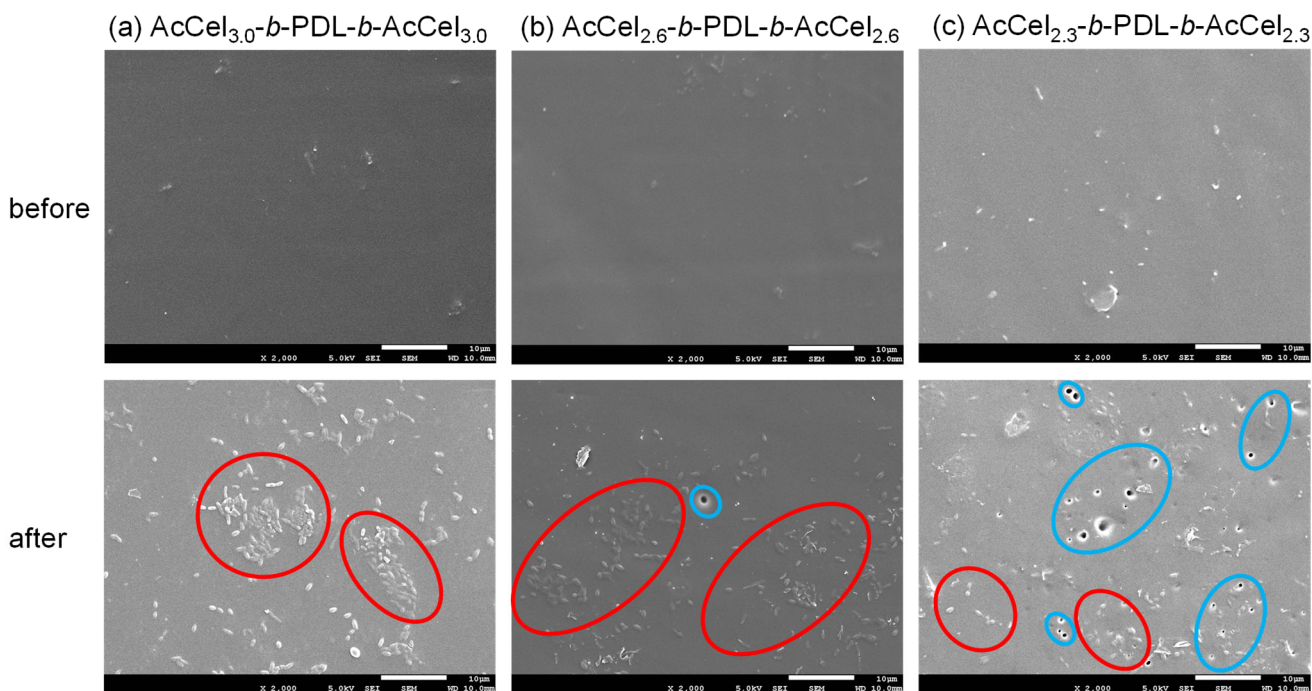
667

668 **Fig. 7.** Stress relaxation curves of AcCel_{3.0}-*b*-PDL-*b*-AcCel_{3.0} (black), AcCel_{2.6}-*b*-PDL-*b*-AcCel_{2.6}
 669 (red), and AcCel_{2.3}-*b*-PDL-*b*-AcCel_{2.3} (blue) at 70% strain.

670 3.6. Biodegradability

671 Cellulose acetate with a lower DS is more susceptible to biodegradation; (Edgar et al.,
 672 2001; Erdal & Hakkarainen, 2022; Kliem et al., 2020; Puls et al., 2011) thus, we investigated the
 673 effect of DS on the biodegradability of AcCel_x-*b*-PDL-*b*-AcCel_x. We performed a preliminary
 674 biodegradability test with the non-annealed AcCel_x-*b*-PDL-*b*-AcCel_x specimens in a recirculating

675 aquaculture system (freshwater environment) in which tilapia had lived for 8 weeks. The water
676 temperature and number of viable bacteria samples were 26 °C and 900 CFU/mL, respectively (for
677 details, see the SI). None of the specimens exhibited an obvious change in appearance, and NMR
678 and SEC analyses revealed no significant changes before and after the biodegradation test (**Figs.**
679 **S21–25**). However, scanning electron microscopy (SEM) observations revealed that
680 microorganisms were adhered to the $\text{AcCel}_x\text{-}b\text{-PDL-}b\text{-AcCel}_x$ film surfaces after the biodegradation
681 test (**Fig. 8**). Interestingly, holes with diameters of $<1\ \mu\text{m}$ were observed in the $\text{AcCel}_{2.6}\text{-}b\text{-PDL-}b\text{-}$
682 $\text{AcCel}_{2.6}$ and $\text{AcCel}_{2.3}\text{-}b\text{-PDL-}b\text{-AcCel}_{2.3}$ films but not in the $\text{AcCel}_{3.0}\text{-}b\text{-PDL-}b\text{-AcCel}_{3.0}$ film. These
683 holes, which were likely formed by a microbial degradation process, indicate that the
684 biodegradation potential increased as the DS decreased. Considering the NMR spectra and SEC
685 results, biodegradation was assumed to proceed only on the surface of the $\text{AcCel}_x\text{-}b\text{-PDL-}b\text{-AcCel}_x$
686 films. Nevertheless, these results demonstrate that biodegradability of $\text{AcCel}_x\text{-}b\text{-PDL-}b\text{-AcCel}_x$ can
687 be improved by simply tuning the DS of the hard segment. However, further long-term tests are
688 required to obtain a comprehensive understanding of this process, and details of the biodegradation
689 behavior in aqueous environments are currently being investigated.



690
691 **Fig. 8.** SEM images of (a) $\text{AcCel}_{3.0}\text{-}b\text{-PDL-}b\text{-AcCel}_{3.0}$, (b) $\text{AcCel}_{2.6}\text{-}b\text{-PDL-}b\text{-AcCel}_{2.6}$, and (c)

692 AcCel_{2.3}-*b*-PDL-*b*-AcCel_{2.3} films before (upper) and after (lower) degradation tests. The red and
693 blue circles show microorganism and newly formed holes, respectively. Scale bars are 10 μ m.

694

695 **4. Conclusion**

696 We used a combination of CDP-mediated celooligosaccharide synthesis, ring-opening
697 polymerization, and a click reaction to synthesize cellulose-based BCPs, AcCel_x-*b*-PDL-*b*-AcCel_x,
698 consisting of celooligosaccharide acetate (AcCel_x) hard segments with three different DSs and only
699 one molecular weight PDL soft segments. The microphase separation behavior and mechanical
700 properties of AcCel_x-*b*-PDL-*b*-AcCel_x were found to be highly dependent on the DS of the AcCel_x
701 segment. In particular, the stronger intermolecular interactions (i.e., hydrogen bonding) associated
702 with decreasing DS positively affected these properties. The findings of this study clearly
703 demonstrate that DS is a useful factor for improving and optimizing the physical properties of
704 cellulose acetate-based TPEs. In addition, we found that the biodegradability of AcCel_x-*b*-PDL-*b*-
705 AcCel_x in an aqueous environment increased as the DS decreased. Although further detailed
706 biodegradation studies are necessary, this tendency is consistent with the fact that cellulose acetate
707 itself is more susceptible to biodegradation when the DS is low (Edgar et al., 2001; Erdal &
708 Hakkarainen, 2022; Kliem et al., 2020; Puls et al., 2011). Overall, DS was found to influence a
709 range of material properties for not only cellulose acetate but also cellulose acetate-based BCPs.
710 This approach can be expanded to the molecular design of a wide range of poly- or oligosaccharide-
711 based BCP materials and will contribute to the development of next-generation environmentally
712 benign polymeric materials that can replace conventional petroleum-based materials.

713

714 **Funding**

715 This work was supported by JSPS Grants-in-Aid for Scientific Research (B) (Nos.
716 19H02549, 20H02792, and 19H02769), the JSPS Fund for the Promotion of Joint International
717 Research (B) (No. 21KK0096), the Japan Science and Technology Agency (JST) COI-NEXT

718 program (Grant Number JPMJPF2102), “Bio-organic Material Recycle System in Space” on MEXT
719 Coordination Funds for Promoting AeroSpace Utilization (Grant Number JPJ000959), the Frontier
720 Chemistry Center (Hokkaido University), the Photoexcitonix Project (Hokkaido University), the
721 Creative Research Institute (Hokkaido University), the Project of Junior Scientist Promotion in
722 Hokkaido University, the Iketani Science and Technology Foundation, the Asahi Glass Foundation,
723 and Toyota Riken.

724

725 **Acknowledgement**

726 This work was, in part, conducted under the approval of the Photon Factory Program
727 Advisory Committee (Proposal nos. 2019G579 and 2021G531). The authors thank Prof. Motomitsu
728 Kitaoka (Niigata University) for providing the pET28a-CDP plasmid, Prof. Hajime Ito (Hokkaido
729 University) for assistance with AFM observations, Mr. Kenji Ohkubo (Hokkaido University) and
730 Mr. Tetsuya Konishi (Hokkaido University) for assistance with SEM observations, and Mr.
731 Hiroyuki Itaya (Kanazawa University) and Ms. Kaoru Kitani (Kanazawa University) for assistance
732 with biodegradation tests.

733

734 **References**

- 735 Bates, F. S., & Fredrickson, G. H. (1990). Block Copolymer Thermodynamics: Theory and
736 Experiment. *Annual Review of Physical Chemistry*, *41*, 525–557.
- 737 Cerqueira, D. A., Valente, A. J. M., Filho, G. R., & Burrows, H. D. (2009). Synthesis and properties
738 of polyaniline-cellulose acetate blends: The use of sugarcane bagasse waste and the effect of
739 the substitution degree. *Carbohydrate Polymers*, *78*, 402–408.
- 740 Crawford, K. E., & Sita, L. R. (2015). *De Novo* Design of a New Class of “Hard-Soft” Amorphous,
741 Microphase-Separated, Polyolefin Block Copolymer Thermoplastic Elastomers. *ACS Macro*
742 *Letters*, *4*, 921–925.
- 743 de Freitas, R. R. M., Senna, A. M., & Botaro, V. R. (2017). Influence of degree of substitution on

744 thermal dynamic mechanical and physicochemical properties of cellulose acetate. *Industrial*
745 *Crops and Products*, 109, 452–458.

746 Edgar, K. J., Buchanan, C. M., Debenham, J. S., Rundquist, P. A., Seiler, B. D., Shelton, M. C., &
747 Tindall, D. (2001). Advances in cellulose ester performance and applicaton. *Progress Polymer*
748 *Science*, 26, 1605–1688.

749 Erdal, N. B., & Hakkarainen, M. (2022). Degradation of Cellulose Derivatives in Laboratory , Man-
750 Made, and Natural Environments. *Biomacromolecules*, 23, 2713–2729.

751 Fournier, L., Rivera Mirabal, D. M., & Hillmyer, M. A. (2022). Toward Sustainable Elastomers
752 from the Grafting-Through Polymerization of Lactone-Containing Polyester Macromonomers.
753 *Macromolecules*, 55, 1003–1014.

754 Grandjean, C., Boutonnier, A., Guerreiro, C., Fournier, J.-M., & Mulard, L. A. (2005). On the
755 Preparation of Carbohydrate-Protein Conjugates Using the Traceless Staudinger Ligation. *The*
756 *Journal of Organic Chemistry*, 70, 7123–7132.

757 Halila, S., Manguian, M., Fort, S., Cottaz, S., Hamaide, T., Fleury, E., & Driguez, H. (2008).
758 Synthesis of Well-Defined Glyco-Polyorganosiloxanes by “Click” Chemistry and their
759 Surfactant Properties. *Macromolecular Chemistry and Physics*, 209, 1282–1290.

760 Hata, Y., & Serizawa, T. (2021). Self-assembly of cellulose for creating green materials with tailor-
761 made nanostructures. *Journal of Materials Chemistry B*, 9, 3944–3966.

762 He, W.-N., & Xu, J.-T. (2012). Crystallization assisted self-assembly of semicrystalline block
763 copolymers. *Progress in Polymer Science*, 37, 1350–1400.

764 Hiraishi, M., Igarashi, K., Kimura, S., Wada, M., Kitaoka, M., & Samejima, M. (2009). Synthesis
765 of highly ordered cellulose II in vitro using cellodextrin phosphorylase. *Carbohydrate*
766 *Research*, 344, 2468–2473.

767 Isono, T., Kawakami, N., Watanabe, K., Yoshida, K., Otsuka, I., Mamiya, H., Ito, H., Yamamoto,
768 T., Tajima, K., Borsali, R., & Satoh, T. (2019). Microphase separation of carbohydrate-based
769 star-block copolymers with sub-10 nm periodicity. *Polymer Chemistry*, 10, 1119–1129.

- 770 Isono, T., Komaki, R., Kawakami, N., Chen, K., Chen, H.-L., Lee, C., Suzuki, K., Ree, B. J.,
771 Mamiya, H., Yamamoto, T., Borsali, R., Tajima, K., & Satoh, T. (2022). Tailored Solid-State
772 Carbohydrate Nanostructures Based on Star-Shaped Discrete Block Co-Oligomers.
773 *Biomacromolecules*, *23*, 3978–3989.
- 774 Isono, T., Komaki, R., Lee, C., Kawakami, N., Ree, B. J., Watanabe, K., Yoshida, K., Mamiya, H.,
775 Yamamoto, T., Borsali, R., Tajima, K., & Satoh, T. (2020). Rapid access to discrete and
776 monodisperse block co-oligomers from sugar and terpenoid toward ultrasmall periodic
777 nanostructures. *Communications Chemistry*, *3*, 1–9.
- 778 Isono, T., Nakahira, S., Hsieh, H. C., Katsuhara, S., Mamiya, H., Yamamoto, T., Chen, W. C.,
779 Borsali, R., Tajima, K., & Satoh, T. (2020). Carbohydrates as Hard Segments for Sustainable
780 Elastomers: Carbohydrates Direct the Self-Assembly and Mechanical Properties of Fully Bio-
781 Based Block Copolymers. *Macromolecules*, *53*, 5408–5417.
- 782 Isono, T., Otsuka, I., Kondo, Y., Halila, S., Fort, S., Rochas, C., Satoh, T., Borsali, R., & Kakuchi,
783 T. (2013). Sub-10 nm Nano-Organization in AB₂- and AB₃-Type Miktoarm Star Copolymers
784 Consisting of Maltoheptaose and Polycaprolactone. *Macromolecules*, *46*, 1461–1469.
- 785 Isono, T., Ree, B. J., Tajima, K., Borsali, R., & Satoh, T. (2018). Highly Ordered Cylinder
786 Morphologies with 10 nm Scale Periodicity in Biomass-Based Block Copolymers.
787 *Macromolecules*, *51*, 428–437.
- 788 Jauzein, T., Huneault, M. A., & Heuzey, M.-C. (2017). Crystallinity and mechanical properties of
789 polylactide/ether-amide copolymer blends. *Journal of Applied Polymer Science*, *134*, 1–10.
- 790 Kamide, K., & Saito, M. (1985) Thermal Analysis of Cellulose Acetate Solids with Total Degrees of
791 Substitution of 0.49, 1.75, 2.46, and 2.92. *Polymer Journal*, *17*, 919–928.
- 792 Kamitakahara, H., Enomoto, Y., Hasegawa, C., & Nakatsubo, F. (2005). Synthesis of Diblock
793 Copolymers With Cellulose Derivatives. 2. Characterization and Thermal Properties of
794 Cellulose Triacetate-Block-Oligoamide-15. *Cellulose*, *12*, 527–541.
- 795 Katsuhara, S., Mamiya, H., Yamamoto, T., Tajima, K., Isono, T., & Satoh, T. (2020).

796 Metallopolymer-*block*-oligosaccharide for sub-10 nm microphase separation. *Polymer*
797 *Chemistry*, *11*, 2995–3002.

798 Katsuhara, S., Takagi, Y., Sunagawa, N., Igarashi, K., Yamamoto, T., Tajima, K., Isono, T., &
799 Satoh, T. (2021). Enhanced Self-Assembly and Mechanical Properties of Cellulose-Based
800 Triblock Copolymers: Comparisons with Amylose-Based Triblock Copolymers. *ACS*
801 *Sustainable Chemistry and Engineering*, *9*, 9779–9788.

802 Kliem, S., Kreutzbruck, M., & Bonten, C. (2020) Review on the Biological Degradation of Polymer
803 in Various Environments. *Materials*, *13*, 4586

804 Kono, H., Hashimoto, H., & Shimizu, Y. (2015). NMR characterization of cellulose acetate:
805 Chemical shift assignments, substituent effects, and chemical shift additivity. *Carbohydrate*
806 *Polymers*, *118*, 91–100.

807 Kuga, T., Sunagawa, N., & Igarashi, K. (2022). Enzymatic synthesis of cellulose in space: gravity is
808 a crucial factor for building cellulose II gel structure. *Cellulose*, *29*, 2999–3015.

809 Liffland, S., & Hillmyer, M. A. (2021). Enhanced Mechanical Properties of Aliphatic Polyester
810 Thermoplastic Elastomers through Star Block Architectures. *Macromolecules*, *54*, 9327–9340.

811 Maji, P., & Naskar, K. (2022). Styrenic block copolymer-based thermoplastic elastomers in smart
812 applications: Advances in synthesis, microstructure, and structure–property relationships—A
813 review. *Journal of Applied Polymer Science*, *139*, e52942.

814 Martello, M. T., Schneiderman, D. K., & Hillmyer, M. A. (2014). Synthesis and Melt Processing of
815 Sustainable Poly(ϵ -decalactone)-*block*-poly(lactide) Multiblock Thermoplastic Elastomers.
816 *ACS Sustainable Chemistry and Engineering*, *2*, 2519–2526.

817 Mumtaz, M., Takagi, Y., Mamiya, H., Tajima, K., Bouilhac, C., Isono, T., Satoh, T., & Borsali, R.
818 (2020). Sweet Pluronic poly(propylene oxide)-*b*-oligosaccharide block copolymer systems:
819 Toward sub-4 nm thin-film nanopattern resolution. *European Polymer Journal*, *134*, 109831.

820 Nishimura, T., Katsuhara, S., Lee, C., Ree, B. J., Borsali, R., Yamamoto, T., Tajima, K., Satoh, T.,
821 & Isono, T. (2022). Fabrication of Ultrafine, Highly Ordered Nanostructures Using

822 Carbohydrate-Inorganic Hybrid Block Copolymers. *Nanomaterials*, *12*, 1–14.

823 Petrović, D. M., Kok, I., Woortman, A. J. J., Ćirić, J., & Loos, K. (2015). Characterization of
824 Oligocellulose Synthesized by Reverse Phosphorolysis Using Different Cellodextrin
825 Phosphorylases. *Analytical Chemistry*, *87*, 9639–9646.

826 Puls, J., Wilson, S. A., & Hölder, D. (2011). Degradation of Cellulose Acetate-Based Materials: A
827 Review. *Journal of Polymers and the Environment*, *19*, 152–165.

828 Pylkkänen, R., Mohammadi, P., Arola, S., De Ruijter, J. C., Sunagawa, N., Igarashi, K., & Penttilä,
829 M. (2020). In Vitro Synthesis and Self-Assembly of Cellulose II Nanofibrils Catalyzed by the
830 Reverse Reaction of *Clostridium thermocellum* Cellodextrin Phosphorylase.
831 *Biomacromolecules*, *21*, 4355–4364.

832 Sarasua, J. R., Arraiza, A. L., Balerdi, P., & Maiza, I. (2005). Crystallinity and Mechanical
833 Properties of Optically Pure Polylactides and Their Blends. *Polymer Engineering and Science*,
834 *45*, 745–753.

835 Serizawa, T., Kato, M., Okura, H., Sawada, T., & Wada, M. (2016). Hydrolytic activities of
836 artificial nanocellulose synthesized via phosphorylase-catalyzed enzymatic reactions. *Polymer*
837 *Journal*, *48*, 539–544.

838 Shin, J., Martello, M. T., Shrestha, M., Wissinger, J. E., Tolman, W. B., & Hillmyer, M. A. (2011).
839 Pressure-Sensitive Adhesives from Renewable Triblock Copolymers. *Macromolecules*, *44*,
840 87–94.

841 Sugiura, K., Saito, M., Sawada, T., Tanaka, H., & Serizawa, T. (2022). Cellodextrin Phosphorylase-
842 Catalyzed Single-Process Production and Superior Mechanical Properties of Organic –
843 Inorganic Hybrid Hydrogels Composed of Surface-Carboxylated Synthetic Nanocelluloses and
844 Hydroxyapatite. *ACS Sustainable Chemistry and Engineering*, *10*, 13484–13494.

845 Sugiura, K., Sawada, T., Tanaka, H., & Serizawa, T. (2021). Enzyme-catalyzed propagation of
846 cello-oligosaccharide chains from bifunctional oligomeric primers for the preparation of block
847 co-oligomers and their crystalline assemblies. *Polymer Journal*, *53*, 1133–1143.

848 Tezuka, Y., & Tsuchiya, Y. (1995). Determination of substituent distribution in cellulose acetate by
849 means of a ^{13}C NMR study on its propanoated derivative. *Carbohydrate Research*, 273, 83–91.

850 Watts, A., & Hillmyer, M. A. (2019). Aliphatic Polyester Thermoplastic Elastomers Containing
851 Hydrogen-Bonding Ureidopyrimidinone Endgroups. *Biomacromolecules*, 20, 2598–2609.

852 Watts, A., Kurokawa, N., & Hillmyer, M. A. (2017). Strong, Resilient, and Sustainable Aliphatic
853 Polyester Thermoplastic Elastomers. *Biomacromolecules*, 18, 1845–1854.

854 Yoshida, K., Tian, L., Miyagi, K., Yamazaki, A., Mamiya, H., Yamamoto, T., Tajima, K., Isono, T.,
855 & Satoh, T. (2018). Facile and Efficient Modification of Polystyrene-*block*-poly(methyl
856 methacrylate) for Achieving Sub-10 nm Feature Size. *Macromolecules*, 51, 8064–8072.

857 Zhou, S. X., Janes, D. W., Kim, C. Bin, Willson, C. G., & Ellison, C. J. (2016). Designing
858 Intrablock Attractions to Increase the χ Parameter of a Symmetric Diblock Copolymer.
859 *Macromolecules*, 49, 8332–8340.

860